Carbon nanocone mechanical behavior and their use as AFM tips for the characterization of polymers in Peak Force mode

Germercy Paredes, C. Villeneuve-Faure, Marc Monthioux

For citing this article:
Paredes G., Villeneuve-Faure C., Monthioux M., Carbon 226 (2024) 119076
https://doi.org/10.1016/j.carbon.2024.119076

Carbon nanocone mechanical behavior and their use as AFM tips for the characterization of polymers in peak force mode

G. Paredes[1 2*], C. Villeneuve-Faure[3*], M. Monthioux[2].

[1] *Laboratorio de Nanociencia, Pontificia Universidad Católica Madre y Maestra, Autopista Duarte Km 1 1/2, Apartado Postal 822, Santiago, Dominican Republic.*
[2] *Centre d'Elaboration des Matériaux et d'Etudes Structurales (CEMES), UPR8011 CNRS, Université Toulouse 3, 29, Rue Jeanne Marvig, BP 94347, 31055, Toulouse Cedex 4, France*
[3]*Laboratoire plasma et conversion d'énergie Université Toulouse 3 - Paul Sabatier, Toulouse, France.*
[*]*Corresponding authors*: gd.paredes@ce.pucmm.edu.do; christina.villeneuve@laplace.univ-tlse.fr

ABSTRACT

Compared to carbon nanotube-based Atomic Force Microscopy probes, carbon nanocone-based probes appear as promising candidates for investigating topography and mechanical properties thanks to the reduced number of artefacts. In this paper, we intend to investigate some of the mechanical features of carbon nanocone (CnC) tips and to evaluate their performances as probes for investigating the mechanical properties of polymer films and composites. Using their force distance curve, the cantilever/CnC spring constant of several CnC probes is determined and the related bending force for each cone is extracted. The results demonstrate CnC bending forces ranging from 100 nN up to 3 µN, which is up to 2 orders of magnitude higher than values reported in the literature for carbon nanotubes. Moreover, the bending phenomenon occurred only when the CnC axis was not strictly perpendicular to the substrate surface. Using Peak-Force Quantitative NanoMechanical (PF-QNM) mode, we demonstrate that CnC probes are suitable to accurately probe polymer mechanical properties, provided the same targeted deformation is used for both the calibration and PF-QNM measurements.

KEYWORDS: Carbon cone, Mechanical characterization, Peak-Force measurements (PF-QNM), AFM probes, bending force, polymer film characterization.

1. Introduction

During the past decades, low-dimensional carbon tips have been proposed for AFM probes [1-3]. In particular, carbon nanotube (CNT)-based AFM probes are extensively investigated due to their ideal features such as nanometer-scale tip radius, high aspect ratio, and bending stiffness [4-6]. These interesting properties were observed for both single-wall (SWCNT) and multi-wall (MWCNT) carbon nanotubes. Compared to standard probes made of silicon, CNT-tips appear

promising to improve lateral resolution due to their small curvature radius [7,8], to probe deep trenches thanks to their high aspect ratio [5,9], to measure thickness of graphene layers [10] or to investigate the surface of soft materials such as biomolecules because of their low bending stiffness [11,12]. These advantages are provided by the intrinsic properties of the carbon material and the related bottom-up manufacturing process [13-15]. In contrast, Si probes manufactured following a top-down process mostly show longer curvature radii (higher than 5 nm) and higher sensitivity to wearing during topography measurement which both limit the lateral resolution [16]. Improving spatial resolution of Si probes is possible by performing some additional steps in order to get sharper tips, but they impact the durability of the probes because of the material brittleness [5,17]. For these reasons, it is almost impossible that Si probes could combine high aspect ratio (*i.e.* tip length over apex radius ratio), high resolution, and high mechanical resistance at the same time. Moreover, MWCNT conductive properties are also interesting for electrical modes derived from AFM as Conductive AFM (C-AFM) [18] or Kelvin Probe Force Microscopy (KPFM) [19]. However, the idyllic expectations of using CNT-tips for surface imaging need to be subdued. For instance, surface mapping in tapping mode suffers from the presence of a lot of artefacts which are closely related to the CNT mechanical properties and the interaction with the surface. Indeed, CNTs could buckle, adhere, slide and/or pin during intermittent contact with the surface inducing unwanted imaging artefacts. Among them, we can cite *(i)* ringing, which appears as parasitic oscillations while the tip is probing abrupt steps [20-22], *(ii)* pit, which consists of a phantom depression around a protrusion on the surface [18], *(iii)* divot, corresponding to a distorted topography profile in the vicinity of abrupt edges [20], *(iv)* error in height measurements [21, 23]. These artefacts are led by a lot of parameters such as CNT geometrical properties (*e.g.* length, curvature radius, deviation angle between the CNT and vertical axes) [9,24], or measurement conditions (*e.g.* the attractive/repulsive force range or the oscillation amplitude) [20]. Consequently, CNT mechanical properties were extensively investigated either theoretically [25] or experimentally [20,23,26,27] in order to suppress these artefacts. This work revealed that probably the most critical parameter is the CNT length, and concluded that a short CNT (less than 500 nm in length) is needed to high-resolution imaging [28]. This implies a trade-off between the high aspect ratio and the lateral flexibility induced by the CNT cylindrical shape [29]. According to the literature overview, two options need to be investigated to overcome these drawbacks. First of all, the surface topography could be probed in Peak-Force tapping mode. Slattery *et al.* [30] demonstrated that Peak-Force tapping avoids the ringing artefact due to the force feedback. However, the pit artefact is still observed. The second option is to use conical instead of cylindrical shapes, *i.e.* nanocones instead of CNTs. Imaging surfaces with conical MWCNTs [31] or carbon cones [32,33] demonstrated no ringing artefact and an improvement of the lateral resolution with an accurate height measurement [31]. Indeed, combining the shape of a cone and the high aspect ratio of a narrow-diameter quasi-cylinder makes conical carbon tips more mechanically stable than CNTs [34-36]. Along with the shape, other important parameters such as the material texture and structure [37] can be controlled by the synthesis method. Many methods, such as Direct Current Plasma Chemical Vapor Deposition (DCP-CVD), Microwave (MW) plasma, and Time of Flight Chemical Vapor Deposition (ToF-CVD) are available for synthesizing conical carbon morphologies [34,38-40]. In particular, all-graphene micro-objects bearing carbon nanocones (CnC) produced by ToF-CVD and then mounted onto cantilevers *via*

micromanipulation demonstrated both suitable geometrical dimensions and shape (*i.e.* needle-like), highly anisotropic texture (co-axial display of the graphene layers), with very high-grade nanotexture (*i.e.* perfect graphene lattices) [37,40,41]. However, investigations on the mechanical properties of CnCs and other conical carbon shapes are scarce in the literature. Indeed, such investigations have been mainly carried-out theoretically, mostly based on molecular dynamics, and focused on unrealistic single-graphene, pentagon-driven cones [42-50]. Only few papers are dedicated to the molecular dynamics modelling of realistic multi-wall cones [29,51,52]. Besides, there is still no agreement on the impact of the geometrical characteristics (length, radius, cone angle) on the bending and/or elastic behavior of graphenic carbon cones. Hence, further experimental work on this subject is necessary to understand better and assess the potential added-value of graphenic carbon cone tips for AFM mechanical characterization.

In this context, by using the specific graphenic CnCs prepared by ToF-CVD already mentioned above [32,33,39-41], this paper aims to investigate the CnC-based AFM tip mechanical properties using the force distance curve (FDC) method and their impact on the determination of polymer material mechanical properties. Experimental results on CnC mechanical behavior are compared using numerical simulation via Finite Element Modelling. In addition, the results described here allow identifying the conditions to perform reliable topographic and mechanical property-measurements. Indeed, it is not straightforward to select appropriate tips for such a purpose, more particularly for ultra-sharp tips. To probe the mechanical properties of polymer films, we used the Peak-Force Quantitative NanoMechanical (PF-QNM) AFM mode due to its promising performance for topography imaging [30].

2. Materials and methods

2.1. Carbon nanocone fabrication process

CnCs used in this work consist of two smooth-surface conical parts supported by a 10-15 µm-long rough-surface microfiber as shown in **Fig. 1a.** The conical parts exhibit a height (h) in the range of 6-7 µm, a width (W) of ~700 nm at the cone base, with a sharp apex radius R_C of 2.2-3 nm, and an apex angle (2α) of around 7°, which makes a quite sharp apex [32,32,41] (**Fig. 1b**).

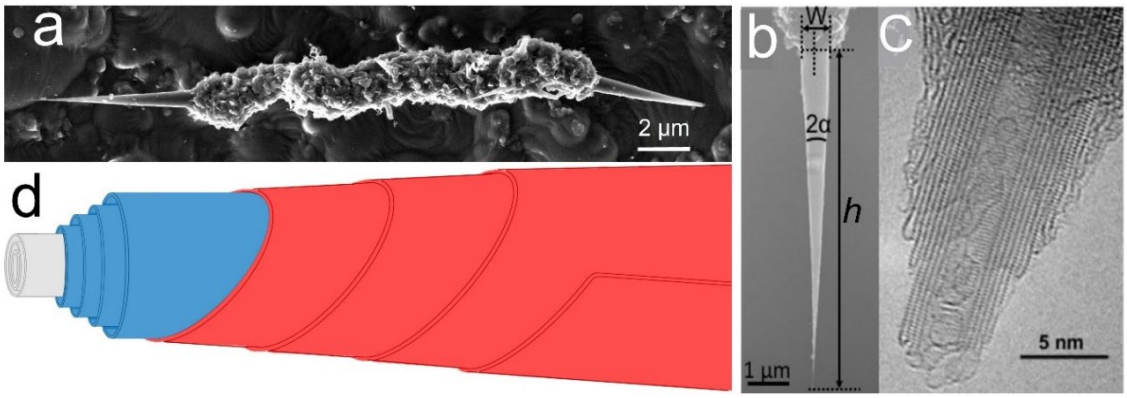

Fig. 1. *Main geometric, textural, and nanotextural characteristics of the ToF-CVD-grown CnCs.* ***(a)*** *Scanning Electron Microscopy (SEM) image of a whole CnC morphology.* ***(b)*** *SEM image showing the*

typical geometric dimensions of one of the cones: length (h) base width (W), and apex angle (2α) of the CnC. ***(c)*** *High resolution transmission electron microscopy* ***(****HRTEM) image showing the graphene perfection (high-grade nanotexture) at the CnC apex. The nanotexture is as perfect also all along the cone length; reprinted from ref [53].* ***(d)*** *Sketch of the dual texture of a cone, i.e. combining both a Russian-doll texture (grey color: the supporting CNT; blue color: the primary CVD-deposited graphene layers) and a multi-scroll texture (red color: the secondary CVD-deposited graphene layers), as discussed in ref. [41].*

These CnCs were synthesized following a ToF-CVD process as detailed in ref. [39]. Briefly, individual carbon cones grow inside a plug-flow reactor from a feedstock of methane (CH_4) and hydrogen (H_2) at high temperature (1400 °C) and atmospheric pressure conditions, following two main steps. In the first step, individual MWCNTs are grown from an iron particle-based catalyst at 1100 °C. These CNTs then are the substrate for the second step, which consists of a two-hour thickening process through pyrolytic carbon CVD deposition, allowing the development of the peculiar morphology illustrated in **Fig. 1a**. Then, the reactor is turned off, and a ballistic (*i.e.* natural) cooling process takes place under inert atmosphere.

Unlike with other CVD techniques, the CnCs resulting from this process do not exhibit metallic nanoparticles at the end, which allows the sharp apex radius observed in **Fig. 1bc** to be obtained. Moreover, this process generates CnCs with very well-defined structural and textural characteristics. They are made of perfect graphene layers which are, for part of them, cylinders concentrically displayed, and for another part, helicoidally wrapped and parallel to the cone axis, thereby making a combination of a scroll texture and a Russian-doll texture [41] as depicted in **Fig. 1d**. In consequence, these CnCs are expected to exhibit promising stiffness properties due to their strong C=C bonding, high nanotexture, and high number of concentric graphenes (up to more than one thousand close to the cone base [41]). In MWCNTs, the bending stiffness actually increases about exponentially with the CNT wall thickness (*i.e.*, with the number of walls [54]).

2.2. CnC-based AFM probe fabrication process

Three whole CnC morphologies were mounted onto customized Sn-doped Si cantilevers with specific profiles, designed by us and then manufactured by AppNano (http://www.appnano.com/home). The mounting process follows either a gluing or a welding procedure as described in ref. [33]. More details about the CnC probes are provided in **Fig. S1** of Supplementary Information (SI). Two of the CnCs were glued onto their cantilever with an ultraviolet (UV)-curable Norland (NOA 68) optical adhesive resin by means of a motorized three-axis micromanipulator (from Micromanipulator Inc.) operated under an optical microscope, equiped with long focal-length objectives and a CCD camera. The resulting probes were named CNC1 and CNC2. The third CnC was welded onto the cantilever with tungsten by means of Focused Electron Beam Induced Deposition (FEBID). The resulting probe was named CNC3. The process required a few cubic-micrometers of $W(CO)_6$ (55% W, 30% C, 15% O) as W precursor, an electron beam energy of 2 keV, and a 200 pA current during few seconds under a dual-beam SEM equipped with a Gemini column and a Schottky-type electron source (ZEISS LEO 1540XB FIB). The latter equipment (operated at 20 kV, hence providing a point resolution of ~1.1nm) was also used to characterize the CnCs once mounted as probes. As a matter of

clarification, it is reminded that, throughout the text, "CnC" is used to designate the carbon micro-objects bearing the carbon nanocones, and "CNC" is used to designate the AFM probe made out of it.

2.3. AFM measurements

AFM measurements were performed using a Bruker Multimode 8 apparatus. The three CNC probes and a standard silicon probe (TESPA-V2 provided by Bruker) were compared. First of all, cantilever and nanocone mechanical behaviors were characterized on both sapphire and TiO_2 substrates using the force-distance-curve procedure (FDC), which depicts the evolution of the force undergone by the AFM probe as function of the tip-sample distance z [55]. An approach and retraction speed of 0.1 µm/s was used for all the measurements. The cantilever static sensitivity S was determined using the slope of the first linear part of the FDC and the spring constant was determined by thermal tune (see section 2 in SI). The maximum force applied on the AFM probe was tuned from 10 nN to few µN to investigate the tip mechanical properties.

Secondly, for investigating the ability of the CNC probes in characterizing accurately the mechanical properties of solid surfaces, various polymer materials were selected: a polystyrene (PS) film supplied by Bruker as a calibration substrate, the Young modulus of which is 2.7 GPa (https://www.brukerafmprobes.com/p-3739-psfilm-12m.aspx); a 50 µm-thick low-density polyethylene (LDPE) film [56]; a 5.8 µm-thick Polyimide (PI) layer deposited by spin-coating on a silicon substrate [57]; and a 40 nm-thick [6,6]-phenyl-C61-methyl butanoate (PCMB) deposited on ITO [58]. The mechanical properties of these polymer layers were assessed in PF-QNM mode [59] at 1 kHz using the three CNC probes and the standard Si probe. All these probes have a spring constant suitable for measuring polymer materials with Young moduli ranging from 1 to 10 GPa. For Young modulus quantitative measurement, a four-step calibration method was applied [57]: *(i)* the cantilever static sensitivity S was determined when investigating the nanocone mechanical properties using the FDC mode on TiO_2 substrate; *(ii)* the probe spring constant k was determined using the "thermal tune" method; *(iii)* the dynamic parameters such as the Sync distance QNM S_d and the peak force tapping (PFT) amplitude sensitivity were determined on TiO_2 using PF-QNM; *(iv)* the tip reduced-radius R^* (see the definition in section 3.1) was calibrated in PF-QNM mode over the PS reference substrate using a deformation target of 2 nm.

Finally, the mapping performances of the CNC probes were investigated on two kinds of composite films: LDPE micro-particles embedded in a PS matrix, supplied by Bruker as a calibration substrate (https://www.brukerafmprobes.com/p-3724-ps-ldpe-12m.aspx), and carbon nanoparticles embedded in a LDPE matrix. This composite film was obtained by mixing (50/50 wt.%) LDPE pellets and carbon blacks (acetylene CB for electrical applications provided by Denka Black) in a Brabender mixer (130°C, 15 rpm, 15 min), then subsequently heat-treating the mixture under pressure (2 tons, 140 °C, 10 min).

2.4. Modelling the mechanical behavior of the carbon nanocones

To investigate the mechanical properties of the carbon nanocones, a simple 3D finite element model (FEM) was developed on COMSOL multiphysics software. As shown on **Fig. 2a**, the nanocone part of a CnC was modelled as a truncated cone (with a base diameter W = 700 nm and a tip-end diameter D_O = 5 nm) with an inner tubular cavity *(*inner diameter D_I = 2 nm [33]) and a length h = 6 µm. These values, as reported in **Table 1**, correspond to typical ones as obtained from SEM observations of several tens of similar as-prepared carbon nanocones.

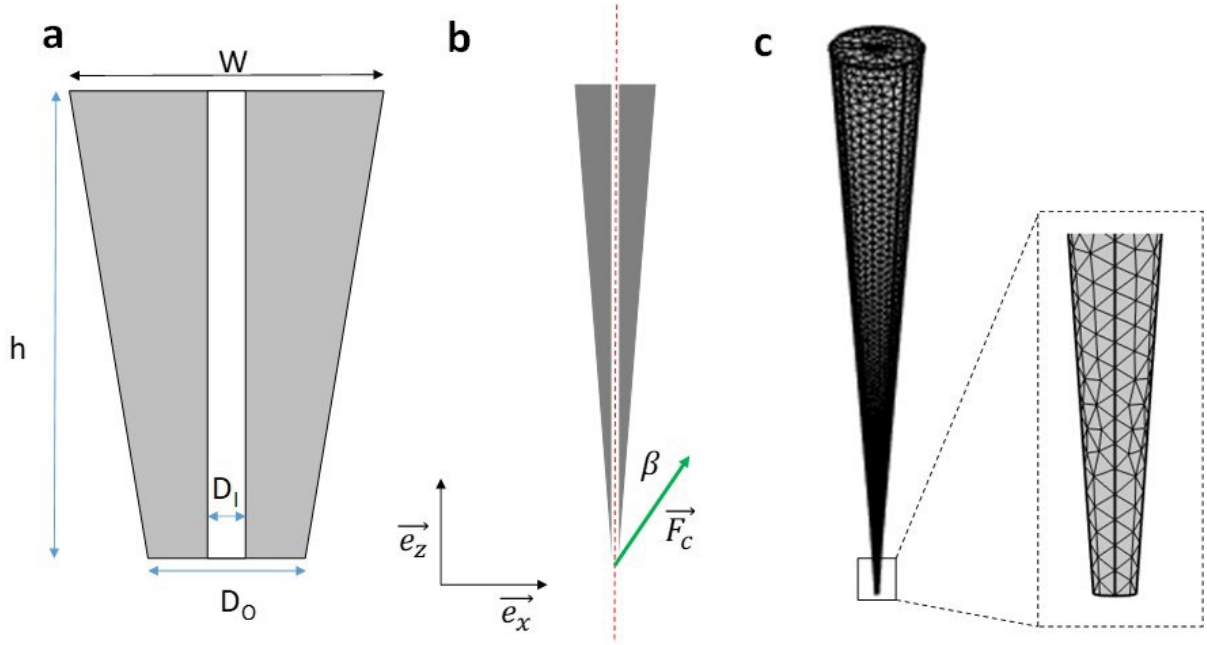

Fig. 2. (a) *Geometrical parameters of the carbon nanocone used in the FEM.* ***(b)*** *3D FEM description and* ***(c)*** *the optimized meshing.*

The mechanical properties of a carbon nanocone are described by the Young Modulus E (unknown) and the Poisson coefficient ν (unknown), with a density $\rho = 2\ 10^3$ kg.m^{-3} [33]. To focus on the mechanical properties of the carbon nanocone, the nature of the contact between the tip and the surface was not investigated. It was modelled in first approximation by the contact force $\overrightarrow{F_C}$ applied to the tip apex (**Fig. 2b**).

Considering only the elastic deformation (the plastic deformation was not considered) for the carbon nanocone, the relationship between stress σ and strain ε is ruled by the Hookes's relation

$$\sigma = E\,\varepsilon \qquad (1)$$

Where E is the Young Modulus of the carbon nanocone.

Moreover, the carbon nanocone deformation was computed using the following relationship

$$\vec{V}(\sigma) + \overrightarrow{F_C} = \vec{0} \qquad (2)$$

where $\overrightarrow{F_C}$ is the contact force.

Two different boundary conditions were considered: a fixed constraint (*i.e.* anchorage) on the carbon nanocone base-edge and a force $\overrightarrow{F_C}$ on the end of the tip (**Fig. 2b**). This force represents the force applied to the AFM tip, and the angle β models the nanocone misalignment with respect to the vertical direction (*i.e.* the direction $\overrightarrow{e_z}$ which is perpendicular to the surface).

β accounts for both the cone axis misorientation angle β' with respect to the direction perpendicular to the cantilever and the cantilever tilt angle due to its enforced position on the AFM tip holder (around 10° for the Bruker multimode 8). An optimized tetragonal mesh was used (**Fig. 2c**) with a minimum element size of 3 nm (and a maximum of 400 nm), a maximum element growth rate of 1.8, and a curvature factor of 0.3.

3. Results and discussion

3.1. CnC-based AFM tip characterization

Fig. 3 shows SEM images of the gluing-processed CNC2 and the welding-processed CNC3 probes, as examples. From such a kind of micrographs, the dimensions and specifications of the three CnCs used for the probes (*i.e.* the height of the cone h and the length of the protruding fiber segment L_f) were estimated and compared with those of the Si tip as summarized in **Table 1.** The height of the conical parts (h in **Fig. 3a**) was in the 5-7 µm range while the overall protruding part (corresponding to the dimensions $L_f + h$ in **Fig. 3b**) is found at around 12 µm for the three probes. The mechanical anchoring of the mounted probes was robust since the dynamic response of the cantilevers only showed a 2 kHz downshift of the resonance frequency due to the added weight of a CnC object (~70 pg) to the cantilever tip [33]. Moreover, CnCs are not perfectly contained in the symmetry plane of the cantilevers and exhibit misalignment angles β' (as part of the angle β shown in **Fig. 2b**) in lateral directions with respect to the vertical direction (**Figs. 3b-d**). The misalignement seems to be more pronounced for CNC3, with an apparent angle $\beta' = 13°$, but the estimation of β' by SEM can be biased in case the image is not taken according to the right view angle and direction.

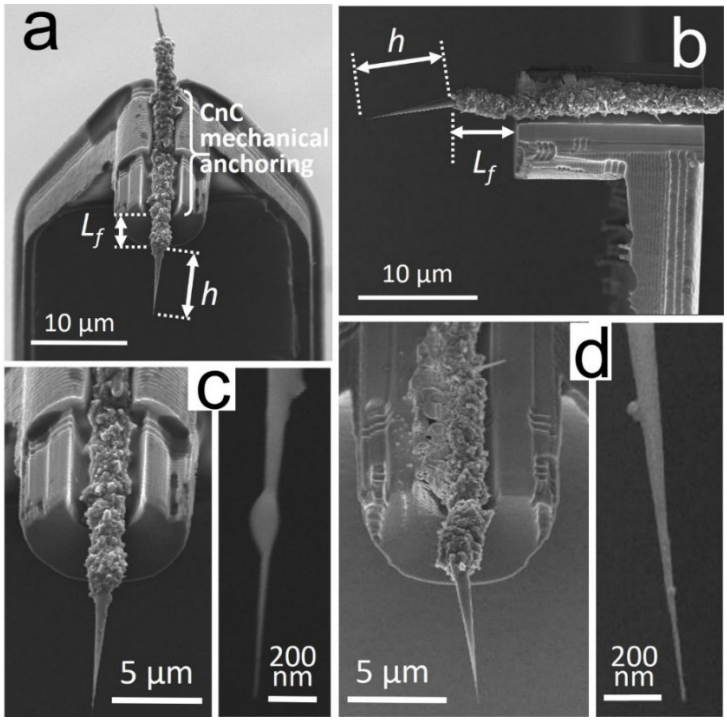

Fig. 3. *SEM images, showing the high aspect ratio of the CnC tips* ***(a)*** *CNC2 and* ***(b)*** *CNC3 after the mounting process. h corresponds to the measured length of the conical part, while L_f is the length of the*

fiber-segment part protruding from the cantilever groove end. ***(c)*** *and* ***(d)*** *SEM images focussing on the end of the cone probe for CNC2 and CNC3, respectively.*

According to SEM images, the cone half-angle is around few degrees (~7°) and the aspect ratio of the mounted probes is ranging from 7:1 to 10:1. Other geometrical characteristics are reported in **Table 1**.

Furthermore, a previous work showed that the CnC probes keep their graphenic nature and structural integrity over the gluing mounting process, but that the structure is increasingly altered (possibly up to amorphisation) when using FEBID and even more when using FIBID (*i.e.* using ions instead of electrons) techniques. [33].

Geometric characteristics	Tips			
	Si (Tespa V2)	CNC1	CNC2	CNC3
Tip height h (µm)	10-15	5.5	6.3	7.2
Fiber protruding length L_f (µm)		5.7	5.2	5
Tip base width W (nm)	ND	710	700	680
Tip curvature radius R_C (nm)	7-10	2-3	2-3	ND
Tip apex angle α	20 ±2.5°	~7°	~7°	ND
Mounting process	NA	Glue	Glue	FEBID

Table 1. Dimension specifications of CnC tips and of the commercial silicon tip. ND = "Not Determined", NA = "Not Applicable".

3.2. Mechanical behavior of carbon nanocone-based AFM tips

To investigate the mechanical properties of carbon nanocones, FDCs obtained on a TiO_2 surface are analyzed. **Fig. 4a** shows the FDC of the standard Si probe. The shape of this curve exhibits only two stages, as expected. During the first stage (labelled (I) in **Fig. 4e**), the tip is not in contact with the surface yet, hence does not exhibit any deformation. After this step, the jump to contact occurred, induced by attractive Van der Waals forces, followed by a deformation of the cantilever (stage (II) in **Fig. 4e**). The static sensitivity S = 41.1 nm/V was determined from stage (II), and a probe spring constant k of 28 N/m was extracted by the "thermal tune" method (see section 2.3, and section 2 in SI). The slope of the curve in stage (II) is 1 nm/nm which implies that the deformation observed is only that of the cantilever beam (*i.e.* the tip-sample distance was corrected from the cantilever deformation using the static sensitivity).

Fig. 4b presents the FDC of the CNC1 probe. The shape of this curve is somewhat similar to that of the standard Si probe, and also exhibits two stages. As previously, the static sensitivity S = 43.5 nm/V was determined in stage (II) for a target deformation of 20 nm, which is close to that of the Si tip, and a probe spring constant k of 20.75 N/m was extracted. However, the attractive force responsible for the jump to contact is weaker. This was previously observed for CNT tips [18,30] and the cause is believed to be similar for the CnC tip, *i.e.* the number of atoms at the CNT or CnC tip apex is lower compared to the standard Si tip apex, which reduces the van der Waals attraction forces. **Fig. 4b** demonstrates that the slope of the curve in stage

(II) remains close to 1 nm/nm, even for a target deformation of 140 nm, which implies that, again, the deformation observed is that of the cantilever beam only.

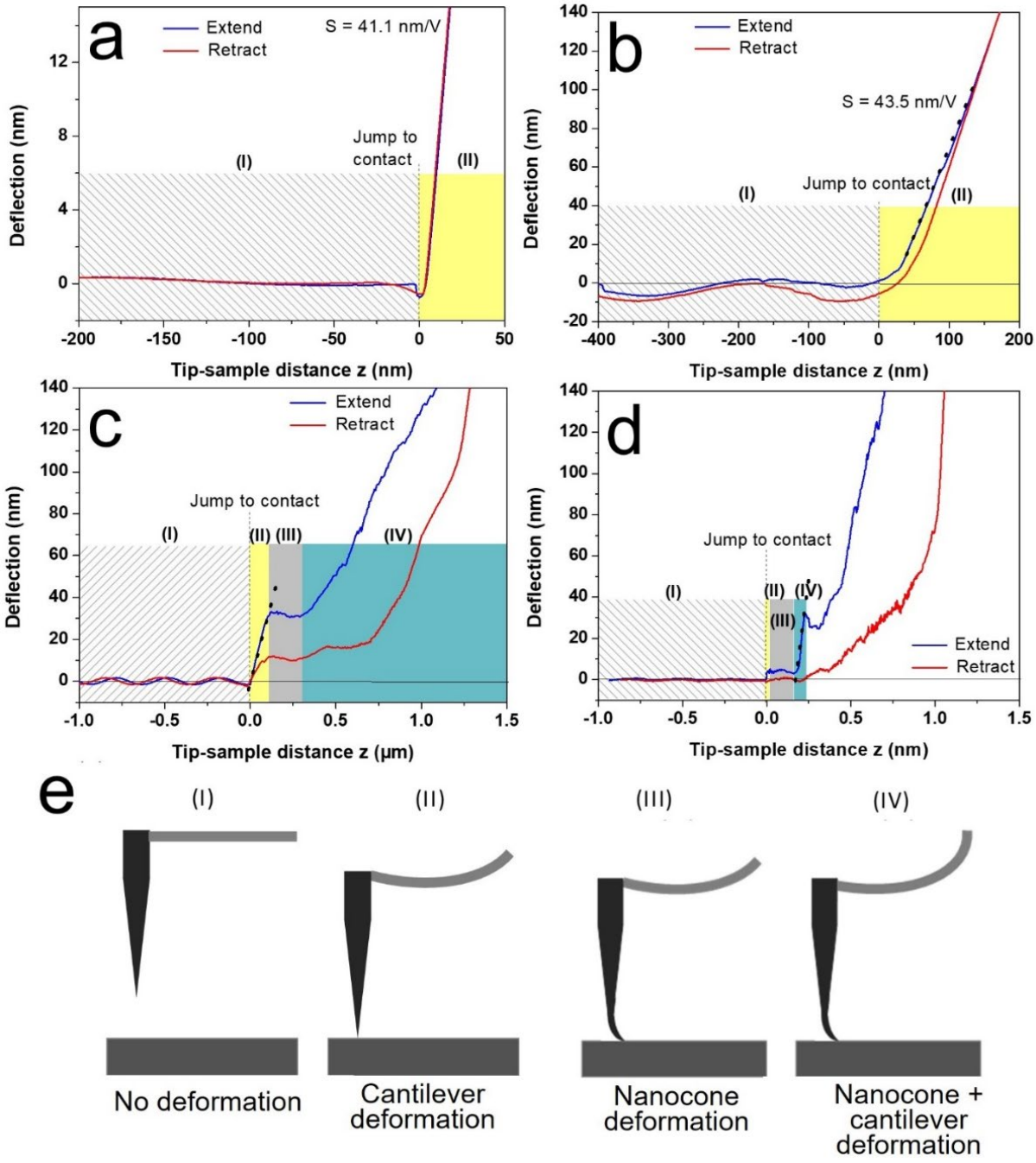

Fig. 4. *FDC obtained on TiO_2 surface for* ***(a)*** *standard Si tip,* ***(b)*** *CNC1,* ***(c)*** *CNC2,* ***(d)*** *CNC3. The tip-sample distance corresponds to the piezo displacement corrected by the sensitivity. The dash line has a slope of 1 nm/nm.* ***(e)*** *Sketch of the motion and behavior of the probe at different stages (the standard 10°-tilt with respect to the perpendicularity to the substrate surface provided to the cantilever by the probe holder is not represented).*

The FDC of the CNC2 probe is more complicated (**Fig. 4c**) as four stages are observed. As previously, the two first stages are attributed to the no-contact zone (stage (I)), and then to the cantilever deformation due to the contact between the CnC tip and the surface (stage (II)). The

static sensitivity S = 57.3 nm/V was determined in stage (II) with a target deformation of 20 nm, and a probe spring constant k of 35.7 N/m was extracted. **Fig. 4c** demonstrates that the slope of the curve in stage (II) remains close to 1 nm/nm, for a deformation up to 31.5 nm. Then, the third stage (labelled (III)) corresponds to a constant cantilever deformation even if the tip-sample distance z decreases. According to the literature, this behavior could be attributed to the carbon-nanocone buckling or bending [21]. As this deformation is progressive (shown by a plateau on the curve), stage (III) is associated to CnC bending as depicted in **Fig. 4e** (Indeed, as buckling is mainly governed by instabilities, it would have induced a sudden decrease of the force). The last stage (labelled (IV)) corresponds to an increase of the cantilever deformation while the tip-sample distance decreases further, with a different slope as compared to stage (II). A plausible hypothesis to explain this behavior is to combine the nanocone bending with the cantilever deformation.

The same behavior as CNC2 is observed for CNC3 (**Fig. 4d**). However, the range of stage (II) is very restricted, and does not permit to extract the static sensitivity accurately. Therefore, the stage (IV) is used to extract the probe sensitivity S of 138.2 N/m and the related probe spring constant k = 6.2 N/m.

For both CNC1 and CNC2 probes, the values for their spring constants k reported above correspond to that of the cantilever beams only, as sensitivity measurements are calculated from stage (II). Concerning the CNC3 probe, the spring constant k corresponds to the combined mechanical properties of both the carbon nanocone and the cantilever (measurement at stage (IV)) and then can be expressed by:

$$\frac{1}{k} = \frac{1}{k_{CnC}} + \frac{1}{k_{cant}} \tag{3}$$

where k_{CnC} and k_{cant} correspond to the CnC and cantilever spring constants respectively (actually, the CnC is here limited to the nanocone part, because it is the only part able to bend and then to act like a spring, as opposed to the short fiber segment part, as sketched in **Fig. 4e**). This is the reason why the spring constant k of CNC3 probe is different from that of CNC1 and CNC2. Indeed, considering equation (3) and a cantilever spring constant k_{cant} of 25 N/m (*i.e.* the mean value of CNC1 et CNC2 spring constant), a k_{CnC} of 8.2 N/m is estimated for CNC3. This value is lower than that of the cantilever which explains the narrow range of the cantilever elastic deformation (*i.e.* stage (II)). Such a low k_{CnC} value may originate from the presumably amorphous nature of the apex of the FEBID-mounted CnC, as discussed below.

Finally, for CNC2 and CNC3, a hysteresis is observed between the approaching and the retracting steps in stages (II), (III) and (IV). This phenomenon, related to energy dissipation, could result either from the nanocone tip friction on the surface which can occurred during tip sliding, or from tip plastic deformation [55]. However, in case the latter explanation is the right one, it cannot come from the cones – provided their structure is unaffected - but possibly from another component of the probe, *e.g.* the welding or gluing materials. Indeed, an interesting observation of the elastic behavior of the nanocone from a CnC was made by an in-TEM experiment during which a CnC was moved toward a solid surface up to contact and beyond, then receded. As presented in **Fig. 5**, a good elastic behavior is observed as the CnC proved to bend by 90° and then to recover its initial shape without any damage. The experiment could be repeated 20 times successively on the same CnC while observing the same behavior. This demonstrates that the strain applied to the cone during PF-QNM experiments, yet severe, is

fully in the elastic domain of the cone material. This confirms a progressive bending-type elastic deformation of the carbon nanocone which occurred at the sharpest part of it.

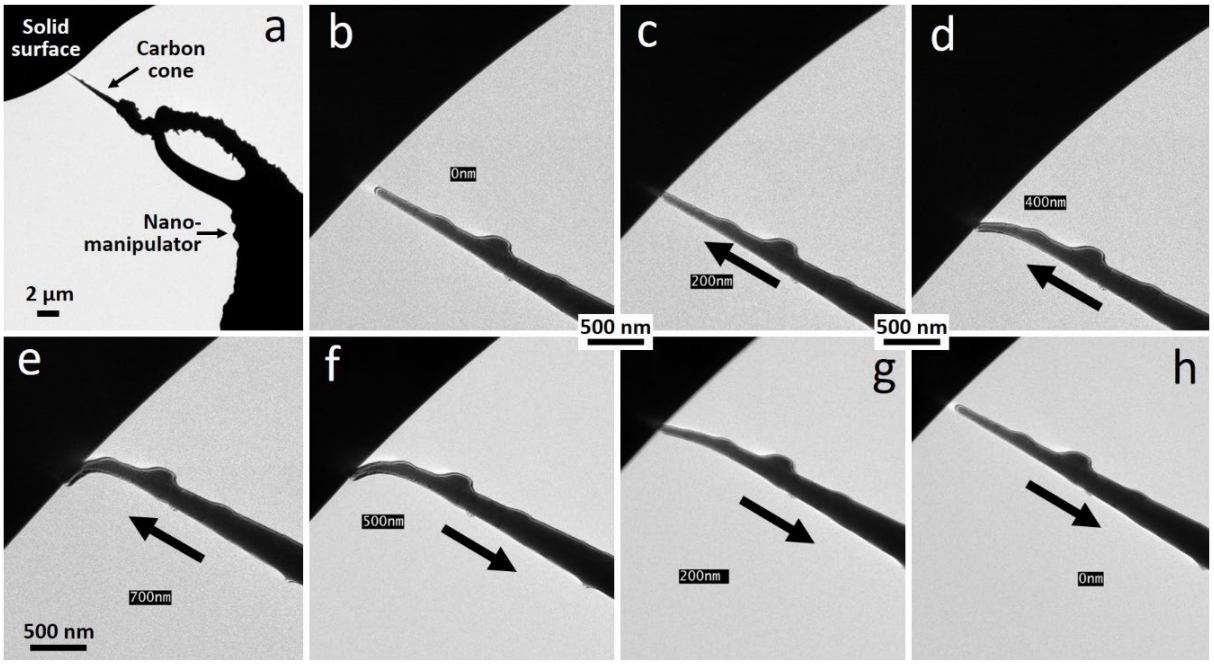

Fig. 5. *In-situ TEM image series (Tecnai F20 operated at 100 kV).* ***(a)*** *Overall view of a CnC mounted onto a TEM sample holder equipped with a nanomanipulator (Nanofactory) positioned in front of a solid surface.* ***(b)*** *to* ***(e)*** *Forward progression of the cone toward the solid surface up to contact, and further. As the CnC keeps moving forward after contact, the contact force increases, resulting ultimately in a 90° bending of the cone.* ***(f)*** *to* ***(h)*** *backward movement of the cone until there is no more contact.*

Moreover, on **Figures 4b-d** at the end of stage (II), the critical force F_B needed to bend the carbon cone is reached and can be evaluated using the following relation

$$F_B = k_{cant}\, \delta_{max}^{ii} \tag{4}$$

where k_{cant} is the cantilever spring constant and δ_{max}^{ii} is the maximum deformation in stage (II). The calculated bending forces F_B are reported in **Table 2**. Even if CNC3 presents a lower bending force than CNC1 and CNC2, these values are higher than those reported in the literature for CNTs. Indeed, for a 5 nm-large and 500 nm-long carbon nanotube, a bending force of 0.05 µN was estimated [25] which is 0.5 to 2 orders of magnitude lower than the 0.1-2.9 µN of the nanocones about 11-12 µm long ($h + L_f$) investigated in this study.

	CNC1	**CNC2**	**CNC3**
$\boldsymbol{k_{cant}}$**(N/m)**	20.8	35.7	≈ 25
$\boldsymbol{\delta_{max}^{ii}}$ **(nm)**	140	31.5	4
$\boldsymbol{F_B}$ **(µN)**	2.9	1.1	0.1

Table 2. *Various characteristics related to the mechanical deformation of the different carbon nanocones, estimated from the FDC.*

CNC1 and CNC2 exhibit bending forces different by a factor of about 3 (2.9 and 1.1 µN, respectively) whereas their geometrical parameters are similar (Table 1), not mentioning the difference by a factor of ~10 to 30 with CNC3 because some of its geometrical parameters are not known. This implies that geometrical parameters are not the most influential parameters on the carbon nanocone bending force. Factors may affect the F_B value, such as differences in the misalignment angle β with respect to verticality (**Figs. 2-3**), or some deviation from conical shape (the occurrence of a solidified glue droplet covering locally the CNC2 cone, as shown on **Fig. 3c**), may locally oppose the bending force, generating a higher F_B with respect to CNC3). Most of all, the 0.5 to 2 orders of magnitude difference of the CNC3 F_B value with respect to CNC1 and CNC2 may reveal a severe structural change of the graphenic carbon material that the cone was initially made with. Indeed, a Raman spectroscopy study of the impact of the mounting process on the CnC structure showed a significant increase of the I_D/I_G ratio, from 0.45 for the glue-mounted CnC (and presumably the pristine CnC as well) to 0.85 for the FEBID-mounted CnC, indicating that the latter has induced defects to the graphene lattice [33]. Furthermore, those ratio values were obtained on the largest parts of the CnCs, *i.e.*, across both the cone-base and the short-fiber-segment, over a material surface thickness of 40-80 nm, corresponding to the penetration depth of the laser probe. Hence, it is clear that the graphene structure was only partially altered in this micrometer-thick probed area, and it is very likely that the structure alteration was much more severe at the thinnest part of the cone, *i.e.* at the apex and the vicinity of it, where diameters are as low as few nanometers. Therefore, the carbon structure of the CnC tip has probably turned from graphenic to amorphous over a significant length of the tip, as it was actually observed when using a FIBID mounting process (*i.e.* using ion beam instead of electron beam) [33]. The characteristics of the resulting amorphous carbon are not known, but its rigidity can be strongly influenced by the sp^2-C/sp^3-C content, as well as any porosity [60]. As a matter of fact, the rigidity of amorphous carbon can be close to 0 for a high sp^2-C content, whereas a Young modulus of ~760 GPa is found for a dense, amorphous carbon with 88% sp^3-C content, both theoretically and experimentally [61,62], to be compared with the value of ~1.1 TPa for multilayer graphene [63].

To investigate the influence of carbon nanocone mechanical properties on bending phenomena, the FEM introduced in section 2.4 will be used. As discussed previously, the carbon nanocone mechanical parameters remain unknown. According to the literature, the carbon nanocone Young Modulus E will range from 200 GPa (amorphous carbon) to 700 GPa (88% sp^3-C content) and to ~1000 GPa (graphene, as well as CNT [64]). The Poisson coefficient was fixed to $\nu = 0.17$ as a mean value compared to those of amorphous carbon (*i.e.* $\nu = 0.15$ for $\rho = 2$ g.cm^{-3}) [65] and of graphene (*i.e.* $\nu = 0.16$-0.46) [66]. Moreover, the misalignment angle with respect to verticality β will range from 0 to 10° (**Fig. 2**). By solving equations (1) and (2) for various contact forces F_C, the carbon nanocone mechanical behavior could be investigated.

Considering a CnC perpendicular to the surface ($\beta = 0$), the deformation occurred only along the z-direction (ε_z) and is located at the extremity of the nanocone (**Fig. 6a**). The vertical deformation increases with the applied force and, as expected, this increase depends on CnC Young modulus (**Fig. 6b**). Whatever the applied force, no bending is observed. Considering FDC measurement, the nanocone vertical deformation ε_z will induce a modification of the slope of the linear part compared to cantilever deformation only. For a cone angle α higher than 5°, no lateral deformation was observed, although the vertical deformation increases as the cone

angle decreases. For a cone angle lower than 4°, lateral deformation occurred with a high amplitude (up to few micrometers for $\alpha = 0°$). As the force is applied along a neutral axis ($\beta = 0°$), this lateral deformation could be associated to buckling. Therefore, a cone angle higher than 4° permits to delay or to avoid the buckling when the force is applied along the cone axis.

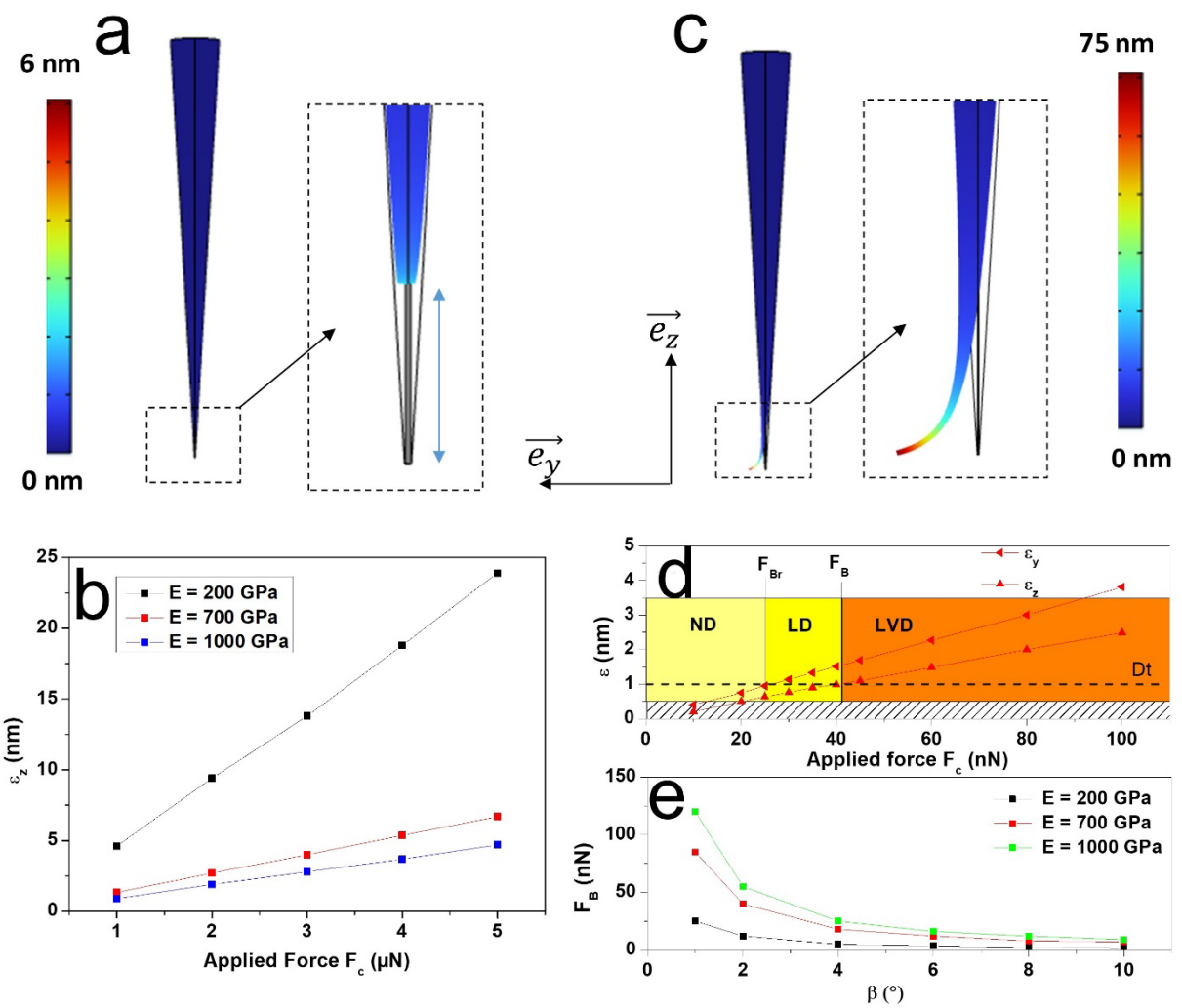

Fig. 6. *Monitoring the deformation of the cone part (E = 700 GPa) of the nanocone through FEM. In (a) and (c), which show the deformed cone, the black-line drawing is a reminder of the original shape.* ***(a)*** *Mapping of the FEM deformation without misalignment (β = 0°).* ***(b)*** *Evolution of the vertical deformation ε_z as function of the applied force F_C for various Young modulus values.* ***(c)*** *Mapping of the FEM deformation of the cone with a misalignment β = 2°.* ***(d)*** *Evolution of the nanocone deformation as a function of the applied force F_C (β = 2°). ND = No Deformation, LD = Lateral Deformation, LVD = Lateral and Vertical Deformation.* ***(e)*** *Evolution of the nanocone bending force F_B as a function of the misalignment angle β for various Young modulus values.*

When a misalignment angle between the CnC and the perpendicular to the surface ($\beta = 2°$) is considered, the nanocone deformation is more complex (**Fig. 6c**). First of all, we can notice that the deformation induced by a contact force of 2 µN is more important for $\beta = 2°$ than for $\beta = 0°$. Secondly, nanocone bending is observed, as well as a deformation in the Y- and Z-directions. The shape and the magnitude of the nanocone deformation simulated by FEM is

similar to that observed experimentally by TEM (**Fig. 5**) as the extremity of the CnC is bended over a height of around 350 nm. The deformation along the Y-direction appears higher than along the Z-direction. This phenomenon is confirmed to depict the evolution of the deformations as function of the applied force (**Fig. 6d**). As the results provided by FEM are driven by macroscale relationships, deformations less than 0.5 nm have no physical signification (shaded area in **Fig. 6d**). Moreover, a detection threshold *Dt* for the deformation was set at 1 nm, this implies that only deformations higher than 1 nm could be detected by FDC. Following the evolution of the deformation as function of the applied force, three behaviors could be identified. For F_C < 22 nN, a non-deformation situation is observed for the CnC (area depicted by "ND" on **Fig. 6d**). For 22 nN < F_C < 40 nN, a lateral deformation (*i.e.* ε_y) is observed whereas no vertical deformation occurred (area depicted by "LD" on **Fig. 6d**). As no vertical deformation occurred, this phenomenon is undetectable on FCD. The nanocone actual bending force F_{Br} corresponds to the lowest force which induces the lateral deformation, which is equal to 22 nN in our case. Finally, for F_C > 40 nN, both lateral and vertical deformations occurred (area depicted as 'LVD" on **Fig. 6d**). The bending force F_B determined using FDC experiments corresponds to the force at the transition between LD and LVD areas. Consequently, nanocone bending occurs before its detection on FDCs and additional FEM results (not shown here) demonstrate that the gap between F_{Br} and F_B decreases with the misalignment angle β. Finally, the bending force decreases with the increase of the misalignment angle β on the one hand, and the decrease of the CnC Young modulus on the other hand.

3.3. Carbon nanocone-based AFM tip for probing polymer mechanical properties

In this part, we aim to evaluate the performances of CnC tips for probing polymer mechanical properties using PF-QNM. Extracting the Young modulus of polymers from PF-QNM measurements is not straightforward as this mode is really sensitive to the calibration process and experimental conditions. In the following, we will focus on the dispersion of the Young modulus measurement and its sensitivity to target deformation. Then we will provide the proof of concept that CnC could be used to probe mechanical properties on both homogeneous and heterogeneous polymers.

To probe mechanical properties, the first step consists of selecting the most suitable model to extract the Young modulus from the fitting of the FDC. According to the determination of the Tabor coefficient (Section 3 in SI), the Derjaguin-Muller-Toporov (DMT) model was preferred to extract the Young modulus of polymer materials [67] using the following relation:

$$E = \frac{3\,(1-\nu_m)}{4\sqrt{R^*}}\left\{\frac{\partial}{\partial z}\left(F_C - F_a\right)^{2/3}\right\}^{3/2} \quad (5)$$

where R^* is the reduced curvature radius, which takes into account the tip radius R_C and the contact surface radius (*i.e.* the radius of the interaction area between the tip and the polymer surface), and which is obtained as explained below; z corresponds to the tip-sample distance, υ is the Poisson coefficient; F_C is the force applied to the tip and F_a is the adhesion force.

Both the Young modulus and the deformation are extracted from the extended part of the FDC. As stated by equation (5), the Young modulus determination depends on the slope of the relation $(F_C - F_a)^{2/3} = f(z)$ and on the reduced curvature radius R^*. So, the accurate measurement of the Young modulus E requires the precise calibration of different parameters.

In previous section 3.2, the static sensitivity S and the spring constant k of the four probes were determined. Then, the parameters specific to PF-QNM measurements were calibrated using a set of force curves measured in peak force mode at 1 kHz on the PS film as reference sample (see section 4 in SI). For PF-QNM calibration and measurements a deformation target of 2 nm was used. This value, commonly taken in the 2-4 nm range, insures that *(i)* deformations remain in the elastic regime (plastic deformation has to be avoided in PF-QNM); *(ii)* the adhesion force is weak (which is needed to be able to use the DMT model according to Tabor parameter – see section 3 in SI); *(iii)* the lateral resolution is improved.

Figs. 7a and **7b** compare the topography image with the Young modulus mapping of PS using the TESPA probe. The PS surface is quite flat with a surface average and a mean root roughness of 0.16 nm and 0.20 nm, respectively. As expected for a homogeneous material as PS, the Young modulus mapping is equable and the weak differences observed are related to small variations of the surface topography.

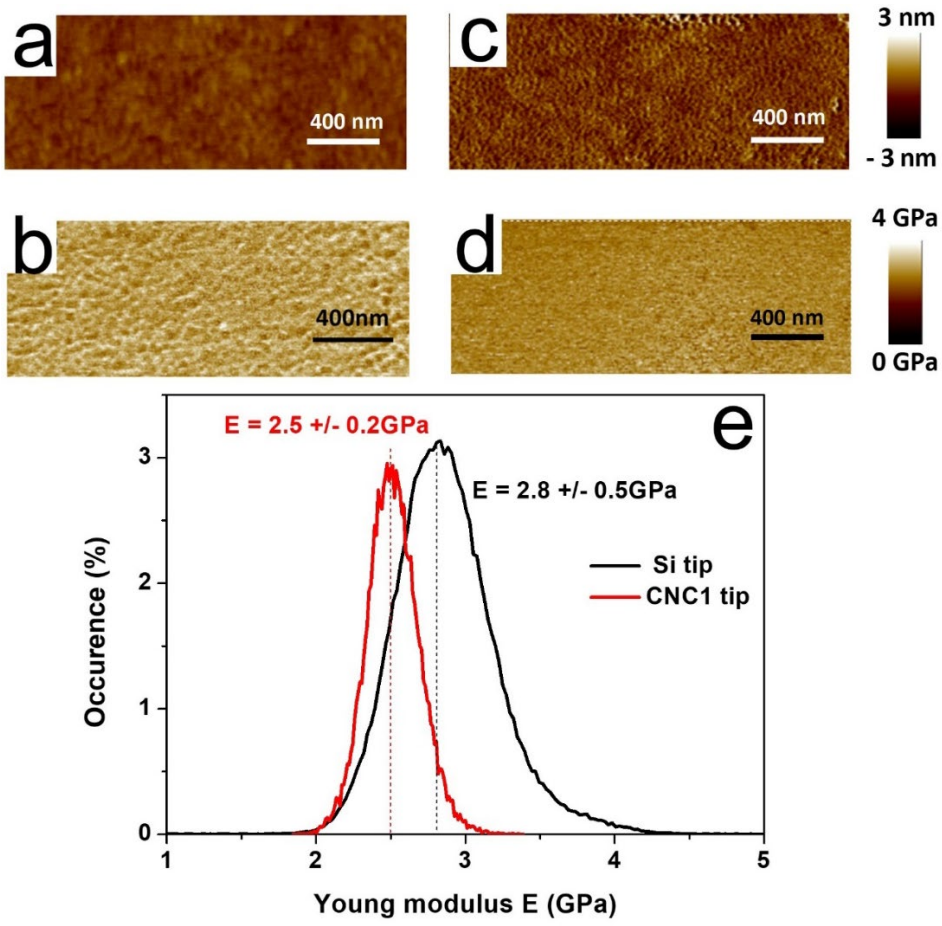

Fig. 7. *1.5 µm x 2 µm PF-QNM images of* ***(a,c)*** *the topography and* ***(b,d)*** *the Young modulus E mapping for the PS sample (contact force F_c = 15.5 nN and deformation target of 2 nm) obtained with* ***(a-b)*** *the standard Si probe and* ***(c-d)*** *the CNC1 probe.* ***(e)*** *Occurrence diagram related to the Young modulus map.*

Figs. 7c and **7d** compare the topography image and Young modulus mapping of PS using the CNC1 probe. The results are similar to those obtained with the Si probe. Indeed, the surface is flat and exhibits a surface average and mean root roughness of 0.34 nm and 0.40 nm, respectively. Moreover, the Young modulus map is equable over the surface. **Fig. 7e** compares the related occurrence diagram for the Young modulus for both the Si and CNC1 probes. Using calibration parameters previously obtained for PF-QNM (section 4 in SI), the Young modulus of PS was determined to 2.8 ± 0.5 GPa and 2.5 ± 0.2 GPa using Si and CNC1 probes, respectively. These values are close to the theoretical one of 2.70 GPa, as provided by the material supplier. Moreover, it is noticeable that the dispersion is lower for the CNC1 probe than for the Si probe, which reveals more repeatable results.

One limitation of the PF-QNM method is the sensitivity of the Young modulus measurement to target deformation. Indeed, as the AFM tip is not ended by a perfect sphere, the reduced curvature radius R^* increases with target deformation (see section 5 in SI), which implies a variation in the extracted Young Modulus (according to equation (5)). To evaluate the relative sensitivity of the CNC and Si probes to target deformation, the evolution of the PS film deformation δ, as extracted from PF-QNM measurements, is followed as function of the contact force F_C in **Fig. 8a** for the standard Si probes and the CNC probes. For the Si, CNC1 and CNC2 probes, a linear relationship is observed between the PS deformation and the contact force which reveals an elastic deformation for the PS layer as predicted by Hook's law. It is a necessary but not a sufficient condition to ensure that those probes are suitable for PF-QNM measurements. Considering CNC3, a nonlinear relationship is observed between deformation and contact force. To explain this non-linear behavior, different hypotheses are available, such as a non-linear carbon nanocone deformation while the PS layer undergoes an elastic deformation, or an instable contact area due to carbon nanocone bending, both possibly related to the intrinsic nature of the nanocone for CNC3 (*i.e.* partial amorphization of the nanocone, as discussed in Section 3.2). As a consequence, this tip appears unsuitable to investigate polymer mechanical properties. **Fig. 8b** demonstrates that the calculated Young modulus increases with the deformation. However, considering a deformation of 2 nm, which corresponds to the target deformation used for R^* calibration, the Young modulus is in agreement with the value provided by the supplier (*i.e.* 2.7 GPa). This phenomenon is related to the fact that R^* value is impacted by the deformation (see section 5 in SI). In this case, when the deformation is lower than 2 nm, the interaction area between the tip and the PS layer presents a diameter lower than $2R^*$. Consequently, the curvature radius is overrated and the Young modulus is lower that the theoretical one (equation (5)). On the contrary, when the deformation is higher than 2 nm, the interaction area between the tip and the PS layer exhibits a diameter higher than $2R^*$. Consequently, the curvature radius in underestimated and the Young modulus is higher than the theoretical one (equation (5)). Moreover, the slope of the linear relation between the Young Modulus and the deformation is similar for the Si and CNC probes. This implies that all probes have the same sensitivity to deformation. Therefore, as for standard Si probes, PF-QNM calibration and measurements need to be carried-out with the same target deformation to ascertain accurate results.

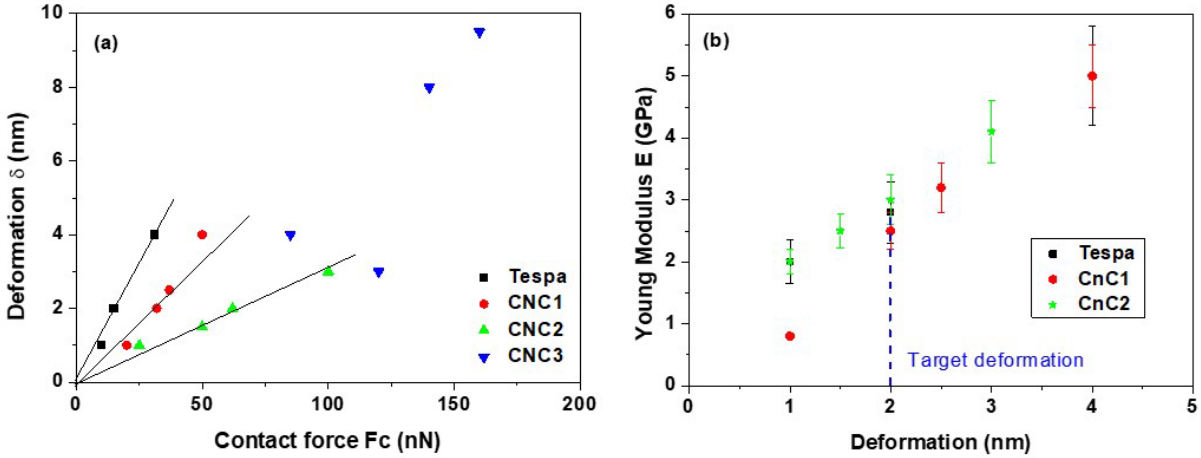

Fig. 8. (a) Evolution of the deformation δ of PS as a function of the contact force *Fc*. **(b)** Evolution of the Young modulus *E* as function of PS deformation δ.

Fig. 9 summarizes the Young modulus measured by PF-QNM on various polymers using the CNC tips. For CNC1 and CNC2 tips, a good correspondence is observed between Young modulus theoretical values and those measured by PF-QNM using a target deformation of 2 nm. Concerning CNC3, the results provided here confirm that this probe exhibits a too low bending force for being suitable to characterize accurately mechanical properties. They also confirm that a dramatic structural modification of the carbon cone resulting from the FEBID process used for preparing CNC3 was very likely. This result is a proof of concept demonstrating that CNC probes with mechanical properties similar to that of CNC1 and CNC2 are suitable to investigate polymer mechanical properties.

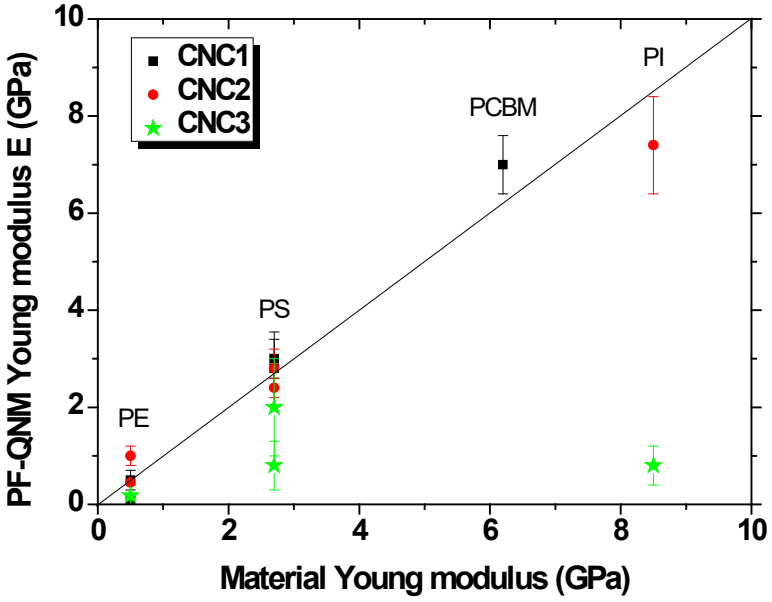

Fig. 9. *Plot of the Young modulus E values for a variety of polymer materials determined by PF-QNM as function of the theoretical ones for different CnC-based probes (the contact force is tuned to reach a deformation target to 2 nm). As these polymers are reference samples for PF-QNM calibration, "Materials Young Modulus" refers to the values provided by the supplier.*

Consequently, to perform reliable mechanical properties measurement using PF-QNM and CnC-based probes two features need to be controlled: *(i)* first of all, a carbon nanocone tip needs to be selected using FDC to ascertain that it exhibits the suitable mechanical properties, *i.e.* a high bending force, so that to avoid nanocone bending and to minimize the contact area. This means that attention has to be paid not to alter the carbon cone structural integrity when processing the probes. For this, it is believed that not using irradiation-based processes (such as FEBID) to mount a CnC onto the support-cantilever should be enough; *(ii)* the same deformation target needs to be used for both the reduced curvature radius calibration and PF-QNM measurement.

Finally, CnC1 was used to map the Young modulus on two different polymer-based composite materials. **Figs. 10a** and **10b** compare the surface topography with the Young Modulus mapping on a composite film composed of micrometer-sized LDPE particles embedded in a PS matrix.

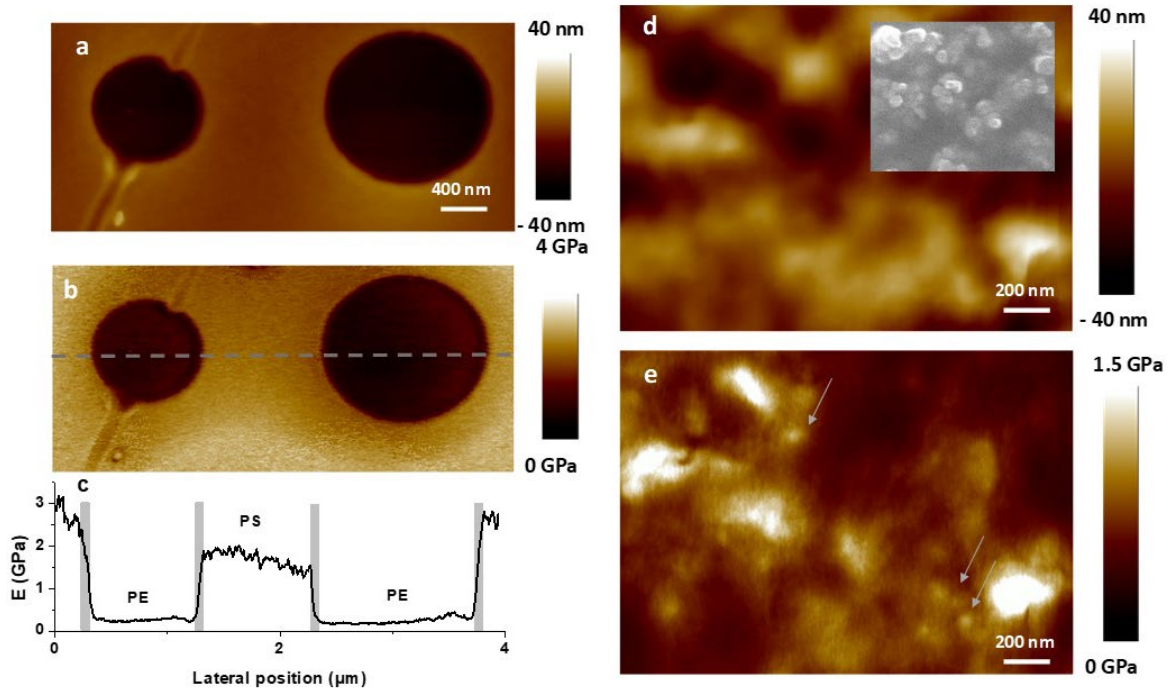

Fig. 10. *CNC1 performance to characterize Young Modulus of polymers by PF-QNM.* ***(a)*** *Surface topography image and* ***(b)*** *Young Modulus mapping of LDPE particles embedded in a PS matrix (applied force of 40 nN for a deformation of 3 nm on PS).* ***(c)*** *Young Modulus profile along the grey dashed line.* ***(d)*** *Surface topography image (inset: SEM image of the same) and* ***(e)*** *Young Modulus mapping of carbon black nanoparticles (some are arrowed) embedded in a LDPE matrix (applied force of 80 nm for a deformation of 2-3 nm).*

The Young modulus profile (**Figs. 10c**) shows a Young modulus of 0.4 GPa for LDPE and between 2 and 3 GPa for PS, which is similar to the values obtained on pristine polymers (**Fig. 9**). The main discrepancy comes from the Young modulus difference (one order of magnitude) which prevents to reach the target deformation of 3 nm with the same contact force for both materials. The width of the transition area between LDPE and PS is around 70 ± 10 nm and increases with the applied force (*i.e.* the target amplitude). Consequently, using a small target

amplitude (around 3 nm) ascertains an optimized condition combining sufficiently high lateral resolution and sufficient deformation to probe accurately the Young modulus. Similar results were obtained with the standard Si probe, however with a larger width of the transition area between LDPE and PS of around 110 ± 10 nm (for the same target deformation of 3 nm). This indicates that the CNC probe seems to provide a better lateral resolution. To confirm this, **Figs. 10d** and **10e** compare the surface topography image and the Young modulus mapping on a nanocomposite formed by carbon black nanoparticles embedded in LDPE matrix. According to SEM imaging (inset in **Fig. 10d**), the carbon black nanoparticles exhibit a diameter ranging from 50 nm to 70 nm. On the Young Modulus map, the CB nanoparticles or clusters of them are well recognized as their Young modulus is higher. Single CB nanoparticles (grey arrows) are observed the dimensions of which - around 80 nm - are consistent with the values obtained by SEM. Using the standard Si probe to map Young modulus variations of this nanocomposite is also able to identify CB nanoparticles indeed, however with apparent diameter ranging from 95 nm to 120 nm. This confirms that the CNC probe provides higher lateral resolution than standard Si-tip on mechanical property mapping.

3.4. Carbon nanocone-based AFM tip wearing

To investigate the morphological and structural evolution of the CnC tips during experiments, they were observed before and after use. The same Si-probe was used to perform 8 FDCs (contact force up to 420 nN) and 6 PF-QNM mappings (with a contact force around 15 nN). SEM observation showed that the apex curvature radius increased from 10 nm before measurement (**Fig. 11a**) to 70 nm after measurement, (**Fig. 11b**), *i.e.* an increase of the apex size by a factor of 7. Compared to the Si probe, CNC2 was subjected to a much more stressful use. Indeed, CNC2 was used to perform 12 FDCs (with contact forces up to 5.2 µN) and 8 PF-QNM mappings (with a contact force around 75 nN). In spite of this, SEM observation showed that the curvature radius increased from 7 nm before measurement (**Fig. 11c**) to 50 nm after experiments (**Fig. 11d**), mostly by shortening the cone, resulting in an increase of the apex size by a factor of ~7 as well, *i.e.* not more than for the Si-tip. Similar results were obtained for CNC3. Moreover, the apex angle remains constant around 7°. The behavior of CNC1 to wear could not be checked because it was deliberately stressed up to breaking.

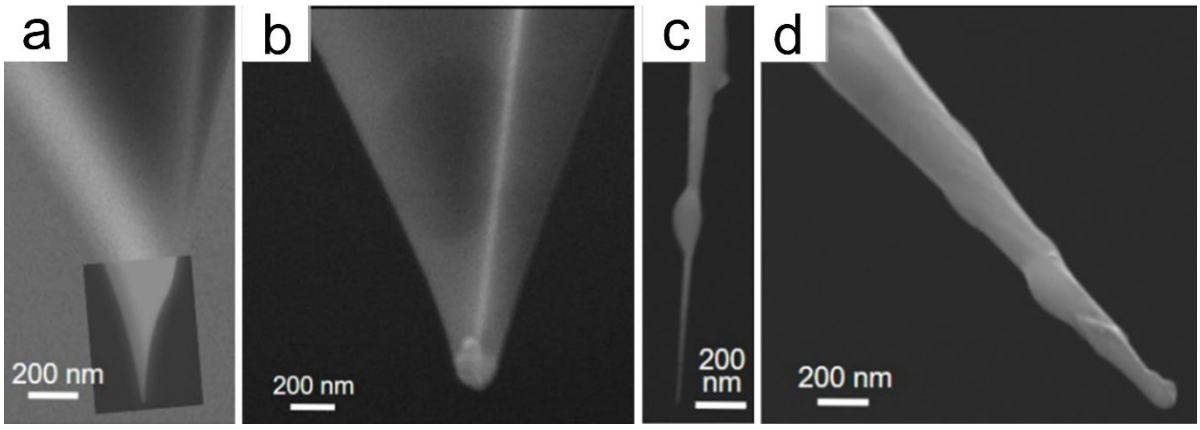

Fig. 11. *SEM observation of Tespa Si-probe* ***(a)*** *before and* ***(b)*** *after FDC and PF-QNM measurements. SEM observation of CNC2* ***(c)*** *before and* ***(d)*** *after FDC and PF-QNM measurements.*

4. Conclusions

In this paper, carbon nanocone-based AFM tips (CNCs) were investigated to probe polymer mechanical properties. First of all, using force distance curve measurements on a TiO_2 film, the nanocone mechanical behaviors were determined regarding their bending force. Bending forces ranging from 100 nN to 3 µN were found, which is up to 2 orders of magnitude higher than values reported in the literature for carbon nanotubes. Moreover, the CNC probe mounted by FEBID (CNC3 probe) exhibited a lower bending force that those which were glued (CNC1 and CNC2). It is shown that this probably relates to the poor mechanical properties of the carbon cone resulting from the structural amorphization of the cone apex induced by the FEBID process. The results obtained by numerical simulation are in a good agreement with the experimental results. Besides, they show that the bending force decreases as the misalignment angle increases and the CNC Young modulus decreases. In addition, the performance of carbon cone-based AFM tips to probe mechanical properties of various polymer layer surfaces was investigated. We demonstrated that, provided the same target deformation is used for both the calibration and PF-QNM measurements, graphenic carbon cones are superior to carbon nanotubes as tips for AFM probes dedicated to this purpose because they exhibit much higher bending forces, and high enough to insure reliable measurements. When compared to standard silicon probes, CNC probes showed a better wear resistance, as expected from the high strength of the C=C bond which their constituting graphenes are made of. Finally, although the comparison with diamond-tip-based probes and amorphous carbon-based probes was not made yet, because diamond-tip probes behave like ceramic materials, *i.e.*, they are brittle, their durability is expected to be low because they are likely to break easily (as brittleness relates to the easiness for a crack to propagate) as opposed to what was shown for our CNC probes (*e.g.*, with **Fig. 5**). On the other hand, the behavior of amorphous carbon-based probes can be anticipated by the results obtained with our CNC3 probe, the carbon cone of which was partly amorphized by the mounting process (FEBID), with which the worse results were obtained. Therefore, none of them are expected to compete with our CNC probes, at least for the PF-QNM investigation of polymers.

Declaration of Competing Interest

The authors declare the following financial interests/personal relationships which may be considered as potential competing interests.

Acknowledgments

This study has been supported through the EUR grant NanoX n° ANR-17-EURE-0009 in the framework of the "*Programme des Investissements d'Avenir*", the CNRS International Research Project NEWCA, and the *Fondo Nacional de Innovación y Desarrollo Científico y Tecnológico* (FONDOCyT), Dominican Republic, Subvención No.2022-1A1-096. The *Pontificia Universidad Católica Madre y Maestra* (Santiago, Dominican Republic) is thanked for providing the PhD grant for GP. Robin Cours (CEMES) is thanked for carrying out the FEBID-assisted nano-welding of the carbon cone (CNC3) showed in **Fig. 3d**. M. Kandara, A.

C. Torres-Dias, and S. Le Blond are thanked for having performed the SEM images. Ludwig de Knoop is thanked for having carried-out the experiment which has resulted in **Fig. 5**.

References

[1] H. Dai, J.H. Hafner, A.G. Rinzler, D.T. Colbert, R. Smalley, Nanotubes as nanoprobes in scanning probe microscopy, Nature 384 (1996) 147-150.

[2] T. Shibata, K. Unno, E. Makino, S. Shimada, Fabrication and characterization of diamond AFM probe integrated with PZT thin film sensor and actuator, Sens. Actuat. A 114 (2004) 398-405.

[3] S. Marsaudon, C. Bernard, D. Dietzel, C.V. Nguyen C, A.-M. Bonnot , J.-P. Aimé, R. Boisgard, Carbon nanotubes as SPM tips: mechanical properties of nanotube tips and imaging, in: Applied Scanning Probe Methods VIII, Nano Science and Technology (Bhushan B., Fuchs H., Tomitori M., eds.), Springer, Berlin, Heidelberg, 2008.

[4] C.P. Collier, Carbon nanotube tips for scanning probe microscopy, in: Carbon Nanotubes Properties and Applications, CRC Press, 2006 (https://doi.org/10.1201/9781315222127)

[5] C.V. Nguyen, Q. Ye, M. Meyyappan, Carbon nanotube tips for scanning probe microscopy: fabrication and high aspect ratio nanometrology, Meas. Sci. Technol. 16 (2005) 2138-2146.

[6] R.M. Stevens, New carbon nanotube AFM probe technology, Mater. Today 12 (2009) 42-45.

[7] C. T. Gibson, The attachment of carbon nanotubes to atomic force microscopy tips using the pick-up method. Appl. Sci. 10 (2020) 5575.

[8] S.K. Kanth, A. Sharma, B.C. Park, W. Song, H. Ruh, J. Hong, Advancement in fabrication of carbon nanotube tip for atomic force microscope using multi-axis nanomanipulator in scanning electron microscope, Nanotechnol. 33 (2023) 175703.

[9] J. Choi, B.C. Park, S.J. Ahn, D.-H. Kim, J. Lyou, R.G. Dixson, N.G. Orji, J. Fu, T.V. Vorburger, Evaluation of carbon nanotube probes in critical dimension atomic force microscopes, J. Micro/Nanolith. MEMS MOEMS 15 (2016) 034005.

[10] C.J. Shearer, A.D. Slattery, A.J. Stapleton, J.G. Shapter, C.T. Gibson, Accurate thickness measurement of graphene, Nanotechnol. 27 (2016) 125704.

[11] L. Chen, C.L. Cheung, P.D. Ashby, C.M. Lieber, Single-walled carbon nanotube AFM probes: Optimal imaging resolution of nanoclusters and biomolecules in ambient and fluid environments, NanoLett. 4 (2004) 1725-1731.

[12] J.E. Koehne, R.M. Stevens, T. Zink, Z Deng, H. Chen, I.C. Weng, F.T. Liu, G.Y. Liu, Using carbon nanotube probes for high-resolution three-dimensional imaging of cells, J. Ultramicrosc. 111 (2011) 1155-1162.

[13] N. Wilson, J. Macpherson, Carbon nanotube tips for atomic force microscopy. Nature Nanotech **4** (2009) 483-491.

[14] A.D. Slattery, A.J. Blanch, J.S. Quinton, C.T. Gibson, Efficient attachment of carbon nanotubes to conventional and high-frequency AFM probes enhanced by electron beam processes, Nanotechnol 24 (2013) 235705.

[15] A.D. Slattery, C.J. Shearer, J.G. Shapter, J.S. Quinton, C.T. Gibson, Solution-based methods for the fabrication of carbon nanotube-modified atomic force microscopy probes, Nanomaterials 7 (2017) 346.
[16] J.L. Mead, W. Klauser, F. von Kleist-Retzow, S. Fatikow, Advances in assembled micro- and nanoscale mechanical contact probes, Front. Mech. Eng 8 (2022) 983334.
[17] L. Guo, R. Wang, H. Xu, J. Liang, Wear-resistance comparison of carbon nanotubes and conventional silicon-probes for atomic force microscopy, Wear 258 (2005) 1836–1839.
[18] A.D. Slattery, C.J. Shearer, C.T. Gibson, J.G. Shapter, D.A. Lewis, A.J. Stapleton, Carbon nanotube modified probes for stable and high sensitivity conductive atomic force microscopy, Nanotechnol. 27 (2016) 475708.
[19] X. Li, X. Hu, M. Liu, L. Sun, X. Qiu, Electrical characteristics of a carbon nanotube-functionalized probe for Kelvin probe force microscopy, J. Phys. Chem. C 124 (2020) 28261-28266.
[20] M.C. Strus, A. Raman, C.-S. Han, C.V. Nguyen, Imaging artefects in atomic force microscopy with carbon nanotube tips, Nanotechnol. 16 (2005) 2482-2492.
[21] M.C. Strus, A. Raman, Identification of multiple oscillation states of carbon nanotube tipped cantilevers interacting with surfaces in dynamic atomic force microscopy, Phys. Rev. B 80 (2009) 224105.
[22] C.V. Nguyen, K.J. Chao, R.M.D. Stevens, L. Delzeit, A. Cassel, J. Han, M. Meyyappan, Carbon nanotube tip probes: stability and lateral resolution in scanning probe microscopy and application to surface science in semiconductors, Nanotechnol. 12 (2001) 363-367.
[23] S.I. Lee, S.W. Howell, A. Raman, R. Reifenberger, C.V. Nguyen, M. Meyyappan, Nonlinear tapping dynamics of multi-walled carbon nanotube tipped atomic force microcantilevers, Nanotechnol. 15 (2004) 416-421.
[24] R. Schlaf, Y. Emirov, J.A. Bieber, A. Sikder, J. Kohlscheen, D.A. Walters, M.R. Islam, B. Metha, Z.F. Ren, T.L. Shofner, B.B. Rossie, M.W. Cresswell, Using carbon nanotube cantilevers in scanning probe metrology, in: Proc. SPIE 27th Annual International Symposium on Microlithography, Santa Clara (CA, USA), 4689 (2002) 493.
[25] B. Cheng, S. Yang, Y.T. Woldu, S. Shafique, F. Wang, A study of the mechanical properties of a carbon nanotube probe with a high aspect ratio, Nanotechnol. 31 (2020) 145707.
[26] S.D. Solares, M.J. Esplandiu, W.A. Goddard, C.P. Collier, Mechanisms of single-walled carbon nanotube probe-sample multistability in tapping mode AFM imaging, J. Phys. Chem. B 109 (2005) 11493-11500.
[27] C. Bernard, S. Marsaudon, R. Boisgard, J.-P. Aimé, Competition of elastic and adhesive properties of carbon nanotubes anchored to atomic force microscopy tips, Nanotechnol. 19 (2008) 035709.
[28] S. Akita, Y. Nakayama, Length adjustment of carbon nanotube probe by electron bombardment, Jpn. J. Appl. Phys. 41 (2002) 4887.
[29] P. Liu, Y.W. Zhang, C. Lu, Molecular dynamics simulations of bending behavior of tubular graphite cones, Appl. Phys. Lett. 85 (2004) 1778-1780.
[30] A.D. Slaterry, C.J. Shearer, J.G. Shapter, A.J. Blanch, J.S. Quinton, C.T. Gibson, Improved application of carbon nanotube atomic force microscopy probes using Peak Force Tapping mode, Nanomater. 8 (2018) 807.

[31] Y. Hu, H. Wei, Y. Dang, X. Chi, J. Liu, J. Yue, Z. Peng, J. Cai, P. Jiang, L. Sun, Amplitude response of conical multiwalled carbon nanotube probes for atomic force microscopy. RCS Advances 9 (2019) 429-434.
[32] G. Paredes, G. Seine, R. Cours, F. Houdellier, H. Allouche, T. Ondarçuhu, F. Plazza, M. Monthioux, Synthesis and (some) applications of carbon-nanotube-supported pyrolytic carbon nanocones, Ind. J. Eng. Mater. Sci. 27 (2020) 1091-1094.
[33] R. Cours, G. Paredes, A. Masseboeuf, T. Ondarçuhu, G. Seine, P. Puech, R. Arenal, F. Piazza, M. Monthioux, New probes based on carbon nano-cones for scanning probe microscopies, Ultramicrosc. 245 (2023) 113667.
[34] Q. Zhang, X.-M. Xie, S.-Y. Wei, Z.-Z. Zhu, L.-S. Zheng, S.-Y. Xie, The synthesis of conical carbon, Small Methods 5 (2021) 2001086.
[35] V.I. Merkulov, M.A. Guillorn, D.H. Lowndes, M.L. Simpson, E. Voelkl, Shaping carbon nanostructures by controlling the synthesis process, Appl. Phys. Lett. 79 (2001) 1178-1180.
[36] V.I. Merkulov, A.V. Melechko, M.A. Guillorn, D.H. Lowndes, M.L. Simpson, Sharpening of carbon nanocone tips during plasma-enhanced chemical vapor growth, Chem. Phys. Lett. 350 (2001) 381-385.
[37] M. Monthioux, Describing carbons, Carbon Trends 14 (2024) 100325.
[38] I.-C. Chen, L.-H. Chen, X.-R. Ye, C. Daraio, S. Jin, C.A. Orme, A. Quist, R. Lal, Extremely sharp carbon nanocone probes for atomic force microscopy imaging, Appl. Phys. Lett. 88 (2006) 153102.
[39] H. Allouche, M. Monthioux, R.L. Jacobsen, Chemical vapour deposition of pyrolytic carbon on carbon nanotubes. Part 1: Synthesis and morphology, Carbon 41 (2003) 2897-2912.
[40] H. Allouche, M. Monthioux, Chemical vapor deposition of pyrolytic carbon on carbon nanotubes. Part 2. Texture and structure, Carbon 43 (2005) 1265–1278.
[41] G. Paredes, R. Wang, P. Puech, G. Seine G, J.-M. Leyssale, R. Arenal, A. Masseboeuf, F. Piazza, M. Monthioux, Texture, nanotexture, and structure of carbon nanotube-supported carbon cones, ACS Nano 16 (2022) 9287−9296.
[42] S.P. Jordan, V.H. Crespi, Theory of carbon nanocones: Mechanical chiral inversion of a micron-scale three-dimensional object, Phys. Rev. Lett. 93 (2004) 255504.
[43] K.M. Liew, J.X. Wei, X.Q. He, Carbon nanocones under compression: Buckling and post-buckling behaviors, Phys. Rev. B 75 (2007) 195435.
[44] P.C. Tsai, T.H. Fang, A molecular dynamics study of the nucleation, thermal stability and nanomechanics of carbon nanocones, Nanotechnol. 18 (2007) 105702.
[45] M.L. Liao, C.H. Cheng, Y.P. Lin, Tensile and compressive behaviors of open-tip carbon nanocones under axial strains, J. Mater. Res. 26 (2011) 1577-1584.
[46] J.X. Wei, K.M. Liew, X.Q. He, Mechanical properties of carbon nanocones, Appl. Phys. Lett. 91 (2007) 261906.
[47] Y.G. Hu, K.M. Liew, X.Q. He, Z. Li, J. Han, Free transverse vibration of single-walled carbon nanocones, Carbon 52 (2012) 4418-4423.
[48] R.D. Firouz-Abadi, H. Amini, A.R. Hosseinian, Assessment of the resonance frequency of cantilever carbon nanocones using molecular dynamics simulation, Appl. Phys. Lett. 100 (2012) 173108.

[49] J.W. Yan, L.W. Zhang, K.M. Liew, L.H. He, A higher-order gradient theory for modeling of the vibration behavior of single-wall carbon nanocones, Appl. Mathem. Model. 38 (2014) 2946-2960.
[50] A. Narjabadifam, F. Vakili-Tahami, M. Zehsaz, M.M.S. Fakhrabadi, Three-dimensional modal analysis of carbon nanocones using molecular dynamics simulation, J. Vac. Sci. Technol. B 33 (2015) 051805.
[51] A. Raj, A. Mokhalingam, S.S. Gupta, Instabilities in carbon nanocone stacks, Carbon 127 (2018) 404-411.
[52] A. Narjabadifam, F. Vakili-Tahami, M. Zehsaz, Elastic and failure properties of carbon nanocones using molecular dynamics simulation, Fuller. Nanotub. Carb. Nanostruct. 26 (2018) 777–789.
[53] P. Puech, M. Kandara, G. Paredes, L. Moulin, E. Weiss-Hortola, A. Kundu, N. Ratel-Ramond, J.-M. Plewa, R. Pellenq, M. Monthioux, Analysing the Raman spectra of graphenic carbon materials from kerogens to nanotubes: what type of information can be extracted from defect bands, 'C' 5 (2019) 69.
[54] S. A. Ponnusami, M. Gupta, D. Harursampath, Asymptotic modeling of nonlinear bending and buckling behavior of carbon nanotubes, in: Proc. AIAA SciTech Forum, January 8-12, Kissimmee (FL, USA), Amer. Inst. Aeronaut.Astronaut., 2018.
[55] H.-J. Butt, B. Cappella and M. Kappl, Force measurements with the atomic force microscope: Technique, interpretation and applications, Surf. Sci. Rep. 59 (2005) 1–152.
[56] F. Gullo, C. Villeneuve-Faure, S. Le Roy, C. Laurent, G. Teyssedre, T.Christen, C.Törnkvist, H. Hillborg, Nano-scale characterization of insulator-semicon contacts, in: Proc. IEEE International Conference on Dielectrics (ICD), 2016, pp.792-795.
[57] M. Houssat, C. Villeneuve-Faure, N. Lahoud Dignat and J.-P. Cambronne, Nanoscale mechanical and electrical characterization of the interphase in polyimide/silicon nitride nanocomposites, Nanotechnol. 32 (2021) 425703.
[58] C. Villeneuve-Faure, D. Le Borgne, E. Bedel-Pereira, K. I. Moineau Chane-Ching, D. Hernandez-Maldonado, I. Séguy, Cross Kelvin force microscopy and conductive atomic force microscopy studies of organic bulk heterojunction blends for local morphology and electrical behavior analysis, J. Appl. Phys. 117 (2015) 055501.
[59] T. J. Young, M. A. Monclus, T. L. Burnett, W. R. Broughton, S. L. Ogin, P. A. Smith, The use of the Peak Force quantitative nanomechanical mapping AFM-based method for high-resolution Young's modulus measurement of polymers, Meas. Sci. Technol. 22 (2011) 125703.
[60] J. Robertson, Diamond-like amorphous carbon, Mater. Sci. Eng. R 37 (2002) 129-281.
[61] A. C. Ferrari, J. Robertson, M. G. Beghi, C. E. Bottani, R. Ferulano, R. Pastorelli, Elastic constants of tetrahedral amorphous carbon films by surface Brillouin scattering, Appl. Phys. Lett. 75 (1999) 1893-1895.
[62] J. W. Suk, S. Murali, J. An, R. S. Ruoff, Mechanical measurements of ultra-thin amorphous carbon membranes using scanning atomic force microscopy, Carbon 50 (2012) 2220-2225.
[63] T. Zhong, J. Li, K. Zhang, A molecular dynamics study of Young’s modulus of multilayer graphene, J. Appl. Phys. 125 (2019)175110.

[64] K.T. Kashyap, R.G. Patil, On Young's modulus of multi-walled carbon nanotubes, Bull. Mater. Sci. 31 (2008) 185–187.
[65] R. Jana, D. Savio1, V. L. Deringer and L. Pastewka, Structural and elastic properties of amorphous carbon from simulated quenching at low rates, Model. Simul. Mater. Sci. Eng. 27 (2019) 085009.
[66] G. Cao, Atomistic studies of mechanical properties of graphene, Polymers 6 (2014) 2404-2432.
[67] M. E. Dokukin, I. Sokolov, On the measurements of rigidity modulus of soft materials in nanoindentation experiments at small depth, Macromol. 47 (2012) 4277-4288.

Carbon nanocone mechanical behavior and their use as AFM tips for the characterization of polymers in peak force mode

G. Paredes[1 2], C. Villeneuve-Faure[3], M. Monthioux[2].

[1] *Laboratorio de Nanociencia, Pontificia Universidad Católica Madre y Maestra, Autopista Duarte Km 1 1/2, Apartado Postal 822, Santiago, Dominican Republic.*

[2] *Centre d'Elaboration des Matériaux et d'Etudes Structurales (CEMES), UPR8011 CNRS, Université Toulouse 3, 29, Rue Jeanne Marvig, BP 94347, 31055, Toulouse Cedex 4, France*

[3]*Laboratoire plasma et conversion d'énergie Université Toulouse 3 - Paul Sabatier, Toulouse, France.*

Supplementary information.

1. Details on the customized CnC-based probes

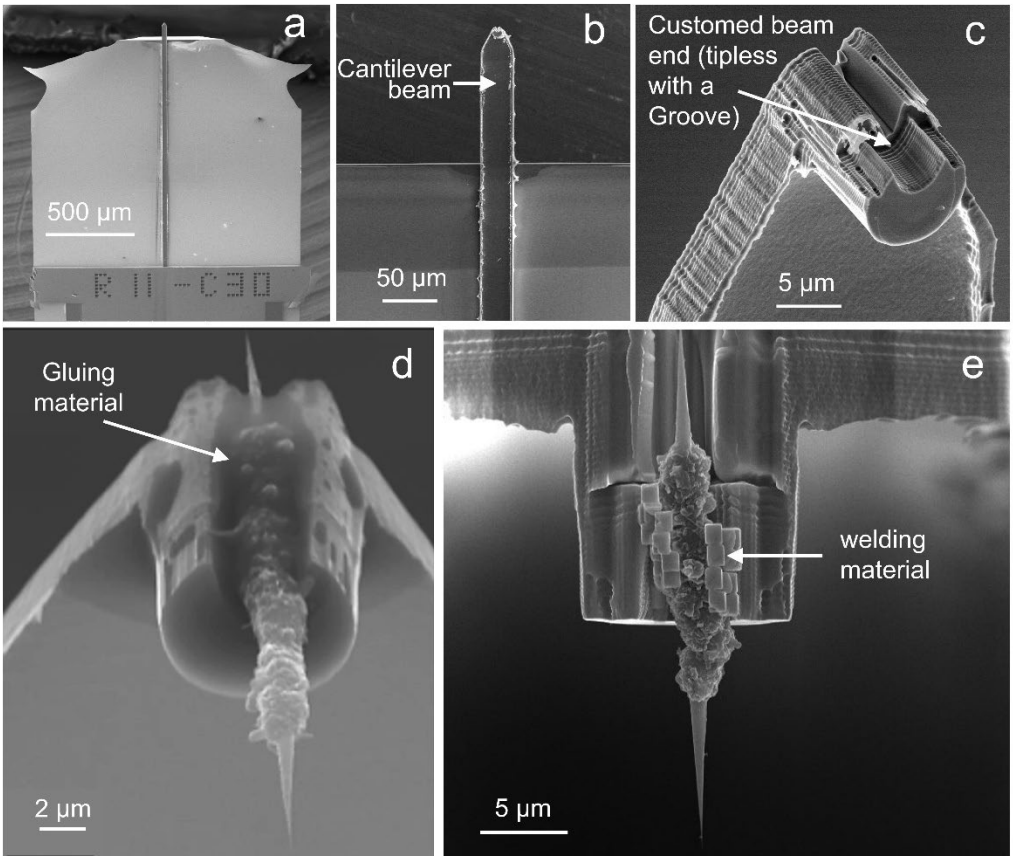

Fig. S1. *SEM images of our customized Si support-cantilever.* ***(a)*** *Low magnification view of half a cantilever (the other half, below the reference number, is that onto which the laser beam reflects.* ***(b)*** *close up of the front part, showing the protruding beam.* ***(c)*** *close-up of the tipless end of the beam, purposely designed to welcome a CnC micro-object (see main text).* ***(d)*** *and* ***(e)*** *CnC-based probes where the CnC is mounted by gluing and by FEBID welding, respectively.*

2. Spring constant and sensitivity calibration

The first step consists in the calibration of the sensitivity of the photodiode-cantilever couple. This could be done in contact or in non-contact mode [1]. As CnC mechanical properties is determined in contact mode, the calibration in contact is preferred. Indeed, the discrepancy between the optical sensitivity determined either in contact or in non-contact mode, which increases with the spring constant [1], could impact the accuracy of FDC measurements and then, the nanocone mechanical property results. The optical sensitivity calibration in contact mode requires the acquisition of a FDC on a stiff surface to reveal the cantilever deformation only. In this study, the sensitivity was calibrated on both a sapphire surface (Young modulus around 350-450 GPa) and a TiO_2 surface (Young modulus around 150-200 GPa) [2].

Regarding the commercial Si probe (*i.e.* Tespa V2), the sensitivity was calibrated on both substrates at 4 different locations and mean values of 41.1 ± 0.5 nm/V and of 41.3± 0.4 nm/V were obtained on TiO_2 and sapphire respectively (target deformation up to 100 nm). This confirms that TiO_2 is a suitable substrate to investigate CnC mechanical properties.

Regarding the calibration of CnC probe sensitivity, the same behavior as the Si probe was observed. However, the reproducibility of the FDC was increased on TiO_2. One hypothesis to explain this phenomenon relates to the higher roughness of the TiO_2 surface (root mean-square roughness of 38 nm over a 5 µm x 5 µm) which minimizes sliding effects. As the objective of this work is to investigate nanocone mechanical properties and not CnC/surface contact, all FDC were performed on TiO_2.

In a second step, the cantilever spring constant is determined by thermal tune. The thermal noise was acquired on a broad frequency range (1kHZ-1MHz) and the resonance peak was fitted with a Lorentzian function (a model adapted to measuring in air). A correction factor of 1.1 was used to take into account the approach angle (*i.e.* the cantilever tilt of around 10° with respect to verticality), the cantilever shape (rectangular) and the tip height (tip height << cantilever beam length). The Si probe spring constant was determined using both the standard thermal tune (k = 26.7 N/m) and the Sader method (k = 28.2 N/m) [3]. This demonstrates a good agreement between both methods, as already demonstrated previously for cantilever spring constants less than 50 N/m [4]. In the following, the spring constant of CNC probes was determined by thermal tune.

3. Selection of the suitable model for determining Young Modulus in PF-QNM mode

To extract the Young modulus from the Force Distance Curve, different models are available, among them the Johnson, Kendall and Roberts (JKR) or the Derjaguin-Muller-Toporov (DMT) models.

As these mechanical property measurements are performed in atmospheric environment (humidity of around 70%), the corrected Tabor coefficient μ_C is considered to determine the most suitable model [5].

$$\mu_C = \left(\frac{2R_C W^2}{9K^2 r_m^3}\right)^{1/3} \quad \text{(S1)}$$

where R_C is the tip radius (provided in **Table 1**) and r_m the radius of the water meniscus, W is the surface energy and K is related to the Young modulus and the Poisson coefficient of both the tip (E_{tip}, ν_{tip}) and the investigated material (E_m, ν_m) by the following relation:

$$K = \frac{4}{3}\left[\frac{1-\nu_{tip}^2}{E_{tip}} + \frac{1-\nu_m^2}{E_m}\right]^{-1} \quad \text{(S2)}$$

Considering standard Si tip, the mechanical properties of silicon is used (E_{tip} = 180 GPa, ν_{tip} = 0.28). Contrary to Si-tip, the mechanical properties of CNC tip is unknown. Therefore, a Young modulus ranging from 700 GPa (88% sp^3C-content) [6,7] to 2000 GPa (about twice that of multi-layer graphene [8]) were considered whereas a Poisson coefficient similar to that of carbon nanotubes is used (ν_{tip} =0.2). Moreover, this range encompasses Young modulus values obtained for either single walled or multi-walled CNT [9].

The surface energy W is related to the pull-off force P_{po} with a relationship which depends on the model considered:

JKR [10]: $$P_{po} = -\frac{3}{2}\pi R_C w \quad \text{(S3a)}$$

DMT [11]: $$P_{po} = -2\pi R_C w \quad \text{(S3b)}$$

As the PS film (E_m = 2.7 GPa, ν_m = 0.35) is used for calibration, this material is also used to evaluate the corrected Tabor parameter μ_C. The pull–off force P_{po} was determined considering the adhesion force F_a of the tip over the PS surface. Results are summarized in **Table S1**.

Considering the Tabor parameter values obtained, the DMT model appears to be the most suited for CnC-tips (*i.e.* $\mu_C < 0.1$) and remains acceptable for Si-tips (*i.e.* $\mu_C << 1$) [4].

Tip	R_c (nm)	E_{tip} (GPa)	ν_{tip}	P_{po} (nN)	μ_C	
					JKR	DMT
Si	8	150	0.28	16±2	0.15 ± 0.01	0.18 ± 0.01
High E nanocone	7	2000	0.2	5.0±0.5	0.090 ± 0.006	0.074 ± 0.006
Low E nanocone	7	700	0.2	5.0±0.5	0.093 ± 0.006	0.075 ± 0.006

Table S1. *Tabor coefficient μ_C determination with two hypothetic CNC probes for measurements on PS (E_m = 2.7 GPa, ν_m =0.35). The radius of the meniscus r_m is taken equal to ~1.2 nm (humidity ratio of 70%).*

4. PF-QNM calibration

The required Peak Force Tapping Amplitude Sensitivity S_{PFT} and the QNM Synchronization distance S_d are extracted from 10 different FDC. These parameters permit to compensate the lag between the vertical motion (*i.e.* the Z motion) and the cantilever deflection. Finally, the reduced curvature radius R^* is calibrated using the PS film as the reference sample. Using a deformation target δ of 2 nm, R^* was adjusted to obtain a Young modulus E_m = 2.8 GPa which is close to the theoretical value (*i.e.* 2.7 GPa for PS). Calibration parameters are summarized in **Table S2**.

	Materials for calibration	Probes			
		Si	CNC1	CNC2	CNC3
Sensitivity *S* (nm/V)	TiO_2	41.1	43.5	46.7	138.2
Spring constant *k* (N/m)	-	25.2	20.8	35.7	6.2
Sync distance QNM S_d	TiO_2	84	75.6	89.7	61.6
PFT Amplitude Sensitivity (nm/V) S_{PFT}	TiO_2	361.5	300.4	255.9	181.5
Reduced radius *R** (nm)	PS	25	25	5	25

Table S2*. CNC and Si tips calibration parameters for PF-QNM measurements. Except for CNC2 probe, R* values are higher than the geometrical curvature radius* R_C *(**Table 1**), which is a common observation, as R* is a combination of the curvature radius and the radius of the interaction area between the tip and the polymer surface. In this context, the fact that R* is similar to* R_C *for CNC2 probe is quite amazing and difficult to explain.*

5. Impact of the deformation target on the reduced curvature radius

The relationship between deformation target and reduce curvature radius *R** is difficult to see for low curvature radius tip, as those used in this study. Indeed, *R** corresponds to the circle radius which fits the contact surface between the probe tip and the polymer material. To illustrate this effect, an Au-coated Si-tip was used (**Fig. S2**). This illustrates that, as the tip apex is not a perfect sphere, *R** increases with the deformation target.

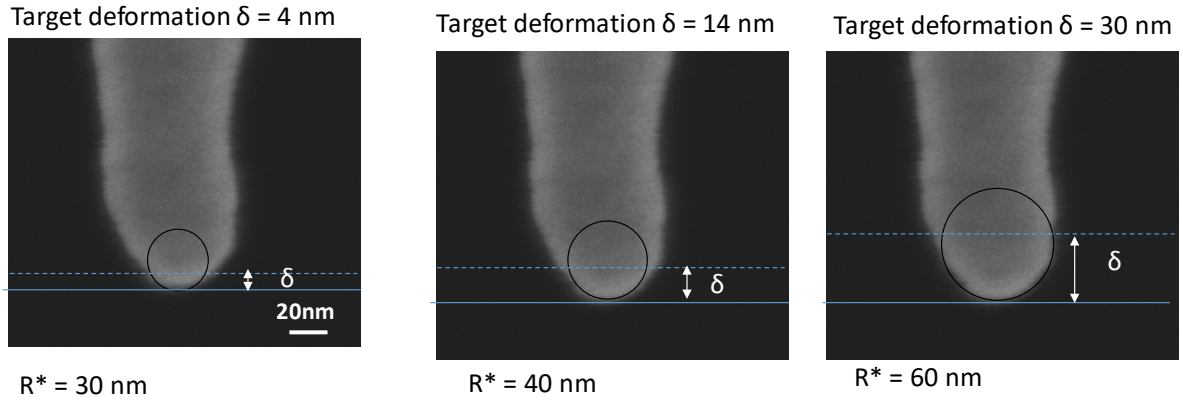

Figure S2. *SEM picture of Au-coated Si-tip and the related reduced curvature radius depending on target deformation.*

References

[1] M.J. Higgins, R. Proksch, J.E. Sader, M. Polcik, S. McEndoo, J.P. Cleveland, SP. Jarvis. Non-invasive determination of optical level sensitivity in atomic force microscopy. Rev. Sci. Instrum. 77 (2006) 013701.

[2] L. Borgese, M. Gelfi, E. Bontempi, P. Goudeau, G. Geandier, D. Thiaudière, L.E. Depero. Young modulus and Poisson ratio measurements of TiO_2 thin films deposited with Atomic Layer Deposition. Surf. Coat. Technol. 206 (2012) 2459.

[3] J.E. Sader, R. Borgani, C.T. Gibson, D.B. Haviland, M.J. Higgins, J.I. Kilpatrick, J. Lu, P. Mulvaney, C.J. Shearer, A.D. Slattery, P.-A. Thorén, J. Tran, H. Zhang, T. Zheng. A virtual instrument to standardise the calibration of atomic force microscope cantilevers. Rev. Sci. Instrum. 87 (2016) 093711.

[4] AD Slattery, JS Quinton, CT Gibson. Atomic force microscope cantilever calibration using a focused ion beam. Nanotechnol. 23 (2012) 285704.

[5] D. Xu, K.M. Liechti, K. Ravi-Chandar. On the modified Tabor parameter for the JKR–DMT transition in the presence of a liquid meniscus. J.Coll. Interf. Sci. 315 (2007) 772-785.

[6] A. C. Ferrari, J. Robertson, M. G. Beghi, C. E. Bottani, R. Ferulano, R. Pastorelli, Elastic constants of tetrahedral amorphous carbon films by surface Brillouin scattering, Appl. Phys. Lett. 75 (1999) 1893-1895.

[7] J. W. Suk, S. Murali, J. An, R. S. Ruoff, Mechanical measurements of ultra-thin amorphous carbon membranes using scanning atomic force microscopy, Carbon 50 (2012) 2220-2225.

[8] T. Zhong, J. Li, K. Zhang, A molecular dynamics study of Young's modulus of multilayer graphene, J. Appl. Phys. 125 (2019)175110.

[9] X. Lu, Z. Hu. Mechanical property evaluation of single-walled carbon nanotubes by finite element modeling. Composites B: Engineering 43 (2012) 1902-1913.

[10] K.L. Johnson, K. Kendall, A.D. Roberts. Surface energy and the contact of elastic solids. Proc. R. Soc. London A 324 (1971) 301-313.

[11] B.V Derjaguin, V.M Muller, Yu. P Toporov,. Effect of contact deformations on the adhesion of particles. J.Coll. Interf. Sci. 53 (1975) 314-326.